Eidgenössische Technische Hochschule Zürich

Ecole polytechnique fédérale de Zurich
Politecnico federale di Zurigo
Swiss Federal Institute of Technology Zurich

Well-balanced high resolution finite volume schemes for the simulation of wave propagation in three-dimensional non-isothermal stratified magneto-atmospheres

F.G. Fuchs*, A.D. McMurry*, S. Mishra and K. Waagan†

Research Report No. 2010-27
September 2010

Seminar für Angewandte Mathematik
Eidgenössische Technische Hochschule
CH-8092 Zürich
Switzerland

*University of Oslo, P.O. Box 1053, Blindern, 0316 Oslo, Norway.
†Unviersity of Maryland, SIC Building 406, College Park, MD 20742-3289, USA.

WELL-BALANCED HIGH RESOLUTION FINITE VOLUME SCHEMES FOR THE SIMULATION OF WAVE PROPAGATION IN THREE-DIMENSIONAL NON-ISOTHERMAL STRATIFIED MAGNETO-ATMOSPHERES.

F. G. FUCHS, A. D. MCMURRY, S. MISHRA, AND K. WAAGAN

Abstract. We consider propagation of waves in a stratified non-isothermal magnetic atmosphere. The situation of interest corresponds to waves in the outer solar (chromosphere and corona) and other stellar atmospheres. The waves are simulated by using a high-resolution, well-balanced finite volume based massively parallel code termed SURYA. Numerical experiments in both two and three space dimensions involving realistic temperature distributions and magnetic field configurations are described, and diverse phenomena like mode mixing, wave acceleration at the transition region, wave focusing due to the magnetic fields and movement of the transition region are highlighted. The numerical experiments illustrate the robustness of the new computational framework. In particular, we are able to report from a simulation based on observed magnetic fields and boundary conditions.

1. Introduction

Waves and oscillations are a significant means for the transport and circulation of energy in gravitationally stratified highly conducting astrophysical plasmas. Examples include waves emitted by localized sources within magnetic flux concentrations such as acoustic sources in the Sun's magnetic network and within isolated magnetic flux tubes, knots and sunspots. Other examples pertain to waves in late type stars and planetary magneto-atmospheres. The study of wave propagation improves our understanding of the dynamical processes in the solar and other stellar atmospheres and contributes to explanations for phenomena like coronal heating and internetwork oscillations.

Consequently, the modeling and simulation of wave propagation in idealized magneto-atmospheres has attracted considerable attention in the astrophysics community. A particular situation of interest in the context of solar physics is to study how convection generated waves transport and deposit energy in overlaying chromospheric and coronal plasmas. Recent papers like [7, 47] have presented simple models for this configuration based on the equations of ideal MHD, augmented by a gravitational source term:

$$\begin{aligned}
\rho_t + \operatorname{div}(\rho \mathbf{u}) &= 0,\\
(\rho \mathbf{u})_t + \operatorname{div}\left(\rho \mathbf{u}\otimes\mathbf{u} + \left(p + \frac{1}{2}\left|\overline{\mathbf{B}}\right|^2\right) I - \overline{\mathbf{B}}\otimes\overline{\mathbf{B}}\right) &= -\rho g \mathbf{e}_3,\\
\overline{\mathbf{B}}_t + \operatorname{div}\left(\mathbf{u}\otimes\overline{\mathbf{B}} - \overline{\mathbf{B}}\otimes\mathbf{u}\right) &= 0,\\
E_t + \operatorname{div}\left(\left(E + p + \frac{1}{2}\left|\overline{\mathbf{B}}\right|^2\right)\mathbf{u} - \left(\mathbf{u}\cdot\overline{\mathbf{B}}\right)\overline{\mathbf{B}}\right) &= -\rho g\left(\mathbf{u}\cdot\mathbf{e}_3\right),\\
\operatorname{div}(\overline{\mathbf{B}}) &= 0,
\end{aligned} \tag{1.1}$$

where ρ is the density, $\mathbf{u} = \{u_1, u_2, u_3\}$ and $\overline{\mathbf{B}} = \{\overline{B}_1, \overline{B}_2, \overline{B}_3\}$ are the velocity and magnetic fields respectively, p is the thermal pressure, g is the constant acceleration due to gravity , $\mathbf{e}_3$ represents the unit vector in the vertical (z-) direction. E is the total energy, for simplicity determined by the ideal gas equation of state:

$$E = \frac{p}{\gamma - 1} + \frac{1}{2}\rho\left|\mathbf{u}\right|^2 + \frac{1}{2}\left|\overline{\mathbf{B}}\right|^2, \tag{1.2}$$

where $\gamma > 1$ is the adiabatic gas constant.

Date: March 16, 2010.

Key words and phrases. Stratified MHD, Non-isothermal atmospheres, Well balanced schemes.

The starting point for wave propagation models based on (1.1) is to determine steady states and consider waves as perturbations of these steady states. Two steady states of interest, considered in [47, 7] and recent papers [20, 22], are

Hydrodynamic steady state. This steady state assumes that the velocity $\mathbf{u}$ and magnetic field $\overline{\mathbf{B}}$ are set to zero. From the ideal gas equation of state, we obtain

$$p = gH\rho T, \tag{1.3}$$

for constant H and T is the temperature. We assume that the steady state temperature $T = T(z)$ varies only in the vertical direction. Substituting (1.3) in (1.1) and assuming $\mathbf{u}, \overline{\mathbf{B}} \equiv 0$ leads to,

$$\frac{dp}{dz} = -\frac{p}{HT(z)}. \tag{1.4}$$

Solving the above equation explicitly yields,

$$p(x, y, z) = p(z) = p_0 e^{-\frac{\alpha(z)}{H}}.$$

Here, p_0 is a constant and

$$\alpha(x, y, z) = \alpha(z) = \int_0^z \frac{1}{T(s)} ds. \tag{1.5}$$

Similarly, we can calculate the steady state density as

$$\rho(x, y, z) = \rho(z) = \frac{\rho_0 T_0}{T(z)} e^{-\frac{\alpha(z)}{H}},$$

with (ρ_0, T_0) being constant. Combining the above expressions, we obtain the following steady state:

$$\mathbf{u} \equiv \mathbf{0}, \quad \overline{\mathbf{B}} \equiv 0 \quad \rho(z) = \frac{\rho_0 T_0}{T(z)} e^{-\frac{\alpha(z)}{H}}, \quad p(z) = p_0 e^{-\frac{\alpha(z)}{H}}. \tag{1.6}$$

Hence, the steady state pressure and density are scaled in terms of the function α which in turn depends on the temperature. Furthermore α is a monotonically increasing function as the temperature is always positive. In the simplest case of an isothermal atmosphere, i.e, $T \equiv \widetilde{T}$ for some constant $\widetilde{T}$, the expression (1.6) simplifies as

$$\mathbf{u} \equiv \mathbf{0}, \quad \overline{\mathbf{B}} \equiv \mathbf{0}, \quad \rho(x, y, z) = \rho_0 e^{-\frac{z}{\widetilde{T}H}}, \quad p(x, y, z) = p_0 e^{-\frac{z}{\widetilde{T}H}}, \tag{1.7}$$

and the pressure and density decay exponentially.

Magnetic steady state. The hydrodynamic steady state assumes that the magnetic field is zero. Any realistic description of solar plasmas cannot ignore the effect of magnetic field since it plays a crucial role in the energy transfer ([7]). Steady states with a magnetic field are easy to determine once the momentum balance in (1.1) is rewritten as

$$(\rho \mathbf{u})_t + \operatorname{div}(\rho \mathbf{u} \otimes \mathbf{u} + pI) = \operatorname{curl}(\overline{\mathbf{B}}) \times \overline{\mathbf{B}} - \rho g \mathbf{e}_3.$$

The above equation displays the role of the Lorentz force explicitly in the momentum balance. Under the assumption that the velocity field is set to zero, the following magnetic steady states are easy to obtain,

$$\begin{aligned} &\mathbf{u} \equiv \mathbf{0}, \quad \operatorname{div}(\overline{\mathbf{B}}) \equiv \mathbf{0}, \quad \operatorname{curl}(\overline{\mathbf{B}}) \equiv 0, \\ &\rho(z) = \frac{\rho_0 T_0}{T(z)} e^{-\frac{\alpha(z)}{H}}, \quad p(z) = p_0 e^{-\frac{\alpha(z)}{H}}. \end{aligned} \tag{1.8}$$

The above conditions require that the magnetic field is both divergence free and curl free. It is easy to obtain closed form solutions of such magnetic fields in terms of harmonic functions ([20, 22] and in section 2). Note that the conditions on steady magnetic fields are quite general and imply that there is a rich variety of magnetic steady states (1.8).

Waves are induced as perturbations of the steady states (1.6) and (1.8). Following [47, 7], we focus on the behavior of waves emanating from spatially localized sources at the bottom vertical ($z-$) boundary. From the discussion of [7] and references therein, a key role is played by the plasma β given by

$$\beta = \frac{2p}{|\overline{\mathbf{B}}|^2}. \tag{1.9}$$

Following [7], one can differentiate between fast and slow magneto-acoustic gravity (MAG) waves in regions of high as well as low β. However, in the *magnetic canopy* characterized by $\beta \approx 1$, the fast, slow and Alfvén waves interact and *mode mixing* may take place. Consequently, the dynamics of wave propagation and energy transport in a stratified magneto-atmosphere is quite complex. The interaction between the waves and the magnetic field as well as the interaction between different wave families in the magnetic canopy needs to be resolved in-order to make qualitative and quantitative predictions for the rates of energy transfer.

In [47, 7], the atmosphere was assumed to be isothermal and the discussion was restricted to two space dimensions. The stratified MHD equations (1.1) were approximated numerically using a staggered finite difference code and the results were analyzed to study mode mixing and dynamics of energy transfer. Detailed analysis of the energy transfer mechanisms was employed to speculate on possible connections to solar phenomena like sunspot, inter and intra-network oscillations. The framework of [47, 7] was simulated with high-resolution finite volume schemes in recent papers [20, 22] and the results of the numerical simulations reinforced the conclusions of [47, 7].

Given the restriction to a two-dimensional isothermal magneto-atmosphere in the afore mentioned papers, it is now time to investigate three dimensional configurations in which the steady state temperature is no longer assumed to be constant. In particular, the outer solar atmosphere is characterized by a vertical steady state temperature distribution shown in figure 1. The temperature is indeed approximately constant over the chromosphere and the isothermal atmosphere assumptions are justified. However, there is a large jump in the temperature distribution from the chromosphere to the corona. This jump is over two orders of magnitude and takes place in the very narrow (when compared to the total length scale) transition region. The coronal temperature varies very slowly and can be approximated by a constant.

The temperature variation in the stratified atmosphere affects wave propagation considerably. In particular, the large temperature jump (in the transition region) will change wave behavior, even in the absence of magnetic fields. When magnetic fields are added to the model, the possible interplay between the transition region and the magnetic canopy might lead to complicated interference of wave forms. Such questions can be resolved by highly accurate direct numerical simulations of the underlying model.

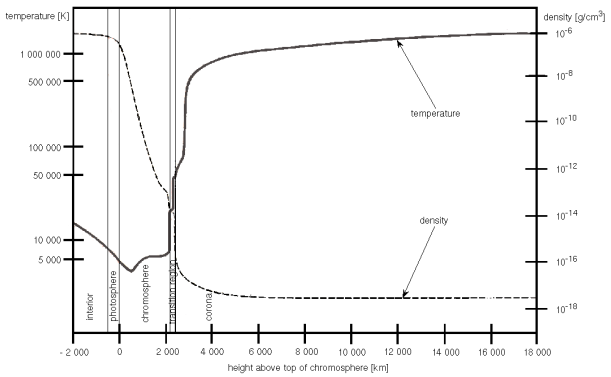

FIGURE 1. Steady state temperature and density distributions in the solar atmosphere. Source: NASA

Similarly, the change from two spatial dimensions ([47, 7, 20]) to three dimensions leads to added complications. The computational cost is increased on account of the extra dimension. More complicated wave forms are

present in three space dimensions and mode mixing might be quite involved. The study of a three dimensional stratified magneto-atmosphere with a realistic steady state temperature distribution is the subject of this paper. The focus is to describe the design of *SURYA* (a high-resolution well-balanced finite volume code) and discuss numerical results obtained with it, in the context of wave propagation in a model of the solar atmosphere. We must emphasize that the physics contained in a simplistic model like the stratified ideal MHD equations (1.1) (even with steady states and boundary data based on observed data sets) is necessarily limited. In particular, energy transfer due to radiation and detailed modeling of the transition region is ignored in the model under consideration. Hence, we do not claim to be able to predict observational results. Rather, this study extends the approach of [47, 7] and focuses on the range of complex phenomena that result from even simple physical models like (1.1). Furthermore, it is highly non-trivial to design a robust numerical framework for (1.1) in three dimensions with our steady state temperature distribution. We describe some of the numerical difficulties below.

1.1. **Numerical issues and literature survey.**

(i.) *Complicated wave structure.* The MHD equations (1.1) are hyperbolic ([46]). The eigenvalues are associated with four wave families: fast, slow, Alfvén and contact (shear) waves. However, the eigenvalues can coincide and the system fails to be strictly hyperbolic. In particular, the fast, slow and Alfvén waves can coincide near $\beta \approx 1$ region. Non-strict hyperbolicity complicates the design of efficient numerical schemes.

Since (1.1) is a system of non-linear balance laws, the solutions develop discontinuities in finite time (even for smooth initial data) in the form of shock waves and contact discontinuities. The structure of shocks and other discontinuities for the MHD equations is quite complicated (see [56] and references therein).

In the absence of explicit solution formulas and a well-posedness theory, numerical simulations are the main tools in the study of systems of balance laws like the MHD equations. Finite volume methods ([32]) are among the most popular numerical methods for approximating non-linear balance laws. The computational domain is divided into control volumes or cells. The method consists of discretizing an integral version of a balance law like (1.1) over each cell to obtain a time update of the cell averages of the unknown. The key step in the update is to determine numerical fluxes by solving local Riemann problems at each cell interface (along the normal direction). The source term in the balance law (1.1) can be discretized in several ways. Higher order accuracy in space can be obtained by using non-oscillatory piecewise polynomial reconstructions like the MUSCL ([58]), ENO ([26]) and WENO ([50]) reconstructions. High order temporal accuracy is obtained by using strong stability preserving Runge-Kutta methods ([25]).

Finite volume schemes for ideal MHD equations have undergone considerable development in the last fifteen or so years. In one space dimension, finite volume schemes for MHD equations include the linearized solvers developed in [46, 11]. Other schemes are the non-linear HLL type solvers designed in [34, 35, 24, 40, 8, 9, 19] and references therein. Some of the HLL type solvers have the added advantage of being positive, i.e., ensuring that the computed pressure and density are positive. Comparisons between different approximate Riemann solvers are performed in papers like [20, 51, 38].

(ii.) *Divergence constraint.* The divergence constraint complicates design of multi-dimensional MHD codes ([57]). Standard finite volume schemes may not satisfy a discrete version of the constraint. This might lead to numerical instabilities in the computations. A number of strategies have been used to handle the divergence constraint in MHD codes. They include the projection method, in which the magnetic field is projected unto a zero divergence field by solving an elliptic equation at each time step ([10]), a method which is computationally expensive. A cheaper alternative is the parabolic cleaning method of [37] and [15].

Another popular method of handling the divergence constraint is the use of staggered grids to ensure that a particular form of discrete divergence is zero. Several versions of staggered grid methods exist, and an incomplete list includes those developed in [3, 2, 14, 17, 36, 49, 48, 51, 55, 57, 30] and other

references therein. A possible disadvantage of staggered grid methods is the complexity of the book-keeping at the code level, leading to overheads in parallelizing the code. It is also more difficult to obtain numerical stability for these schemes, since some of the theoretical basis of finite volume schemes is lost.

An alternative divergence cleaning procedure was presented in [44, 45] where a slightly different form of the ideal MHD equations (with a source term proportional to divergence) was discretized. This form, also called the *Godunov-Powell* form happens to be symmetrizable ([23]) and Galilean invariant. Furthermore, in the Godunov-Powell form divergence errors are transported out of the domain with the flow ([44]). Similar ideas were presented in [15]. A possible pitfall of this procedure was pointed out in [18, 19, 21]. Examples were presented to argue that the Godunov-Powell form needs to be discretized in a suitable manner for numerical stability. Various upwind discretizations of a partial form of the Godunov-Powell source term were proposed recently in [8, 59, 19].

The Godunov-Powell form makes it mathematically feasible to deal with data not satisfying the divergence constraint. Hence, it allows constructing one-dimensional schemes that immediately extend to accurate and remarkably robust multidimensional schemes, as carried out by the authors in [21] and [59]. The method involved designing suitable three- and five wave HLL type solvers such that the Godunov-Powell source term could be discretized in an upwind manner. Positivity preserving high order ENO and WENO reconstructions were also proposed. The resulting schemes were high order accurate and robust in computations, particularly on very fine meshes. The numerical schemes designed in [21] constitute an attractive framework for robust simulations of models involving MHD equations. We will extend the approach proposed in [21] for discretizing (1.1)

(iii.) *Well-balancing.* The balance law (1.1) involves the gravity source term in addition to the ideal MHD equations. The steady states (1.6) and (1.8) are of great interest in the computations as the waves are realized as small perturbations of these steady states. Hence, it is crucial to *preserve* suitable discrete versions of (1.6) and (1.8). Standard finite volume schemes are not designed to preserve discrete steady states and may lead to large errors (particularly for long time scales). Furthermore, these numerical errors might be of the same size as the waves, making resolution of waves impossible, except on very fine meshes. In [20], we presented some of the difficulties associated with the lack of *well-balancing* in finite volume schemes for (1.1).

We term schemes that preserve discrete versions of the steady states (1.6) and (1.8) as *well balanced*. The design of well-balanced schemes for systems of balance laws like the shallow water equations with bottom topography and Euler equations for gas flows in a nozzle have received considerable attention in the literature (see [1, 12, 29, 31, 41, 42] and other references therein). However, very few well-balanced schemes for stratified hydrodynamics and MHD are available. In a recent paper [22], we designed high-resolution well-balanced schemes for the two-dimensional form of the stratified MHD equations (1.1) under the assumption that the steady state was *isothermal* (1.6). The two key steps in the design was to use an equivalent form of (1.1) with the perturbation to the background field as the magnetic primary variable, and to employ novel *equilibrium preserving* hydrostatic reconstructions of the conserved variables. The resulting scheme was successful in resolving waves as perturbations of realistic isothermal magneto-atmospheres.

(iv.) *Non-reflecting boundary conditions.* Since we are interested in a small part of the solar atmosphere, periodic boundary conditions are prescribed for the horizontal boundaries. The bottom vertical (z-) boundary is the source of waves and time-dependent Dirichlet boundary conditions needs to be prescribed for it. Due to the truncation of the computational domain, the top boundary is artificial and suitable *non-reflecting* numerical boundary conditions need to be designed.

The design of non-reflecting numerical boundary conditions has received widespread attention in the literature. Characteristic boundary conditions ([43, 54]) are quite popular in gas dynamics codes. However, these boundary conditions are observed to be unstable for the stratified MHD equations on account of failure to preserve positive pressures and densities (see [20] for counter examples and explanation). Furthermore, the boundary conditions need to be well-balanced i.e, they should also lead to a discrete version of the steady state to be preserved. A class of "non-reflecting" Neumann type

numerical boundary conditions was proposed recently in [22], based on a novel extrapolation of the equilibrium variables at the ghost cells in-order to ensure well-balancing.

1.2. **Scope and content of the paper.** In [22], the authors tackled all the afore mentioned issues to design a robust high-order accurate finite volume scheme for discretizing the stratified MHD equations. The schemes approximated an equivalent form of (1.1) that embedded the steady magnetic field as a co-efficient in the equations. This form was also proposed in a different context in [53, 45]. The Godunov-Powell form of the ideal MHD equations was discretized by an HLL three wave solver (proposed in [21]). Second-order of accuracy was recovered using non-oscillatory minmod, ENO and WENO reconstructions. Well-balancing was achieved by a novel reconstruction procedure involving local equilibria. Neumann type numerical boundary conditions led to low amount of reflections at the top boundary. Numerical experiments illustrating the robustness of the approach and reinforcing the conclusions of [7] were presented.

However, [22] considered only isothermal atmospheres and the numerical results were restricted to two space dimensions. We extend the numerical framework of [22] to cover non-isothermal three dimensional magneto-atmospheres in this paper. In terms of the algorithm, the key difference from [22] is the use of a *novel local reconstruction of the pressure*, based on the scaling function α (1.5), that allows us to preserve discrete versions of *any* non-isothermal steady state (1.6) and (1.8). Furthermore, a structural property of the numerical fluxes is identified that enables any consistent reconstruction of the density, velocity and magnetic fields to be coupled with the *hydrostatic* pressure reconstruction for obtaining a well-balanced scheme.

The schemes are implemented in the form of a scalable, massively parallel, C++ based code termed *SURYA*([52]). The code is scheduled for public release and contains a wide variety of approximate Riemann solvers, reconstruction routines and well-balancing sub-modules. *SURYA* is employed to investigate wave propagation in non-isothermal magneto atmospheres. The basic two-dimensional configuration of [47, 7] is augmented by a realistic temperature distribution approximating the one shown in figure 1. Furthermore, we present numerical results for three-dimensional stratified magneto-atmospheres. The magnetic field configuration of [47, 7] is extended to three-dimensional potential fields. The results are discussed in terms of the physics of mode mixing, interactions of wave families and the role that the transition layer and the temperature jump play in the transport of energy by waves and the resulting movement of the transition layer. In-order to demonstrate the robustness and range of applicability of the code, we will report results from a simulation of waves with an *observed* background magnetic field and basal boundary condition.

The rest of the paper is organized as follows: In section 2, we present an equivalent Godunov-Powell form of (1.1) (with embedded steady states). Explicit forms of the steady magnetic field in both two and three space dimensions are also presented. The well-balanced high-resolution finite volume scheme is presented in section 3. Two and three dimensional numerical results are presented in sections 4 and 5 respectively and the contents of this paper are summarized in 6.

2. The Model

The *semi-conservative* Godunov-Powell form of the stratified MHD equations ([45]) are,

$$
\begin{aligned}
\rho_t + \operatorname{div}(\rho \mathbf{u}) &= 0, \\
(\rho \mathbf{u})_t + \operatorname{div}\left(\rho \mathbf{u} \otimes \mathbf{u} + \left(p + \frac{1}{2}\left|\overline{\mathbf{B}}\right|^2\right) I - \overline{\mathbf{B}} \otimes \overline{\mathbf{B}}\right) &= -\overline{\mathbf{B}}(\operatorname{div}\overline{\mathbf{B}}) - \rho g \mathbf{e}_2, \\
\overline{\mathbf{B}}_t + \operatorname{div}(\mathbf{u} \otimes \overline{\mathbf{B}} - \overline{\mathbf{B}} \otimes \mathbf{u}) &= -\mathbf{u}(\operatorname{div}\overline{\mathbf{B}}), \\
\overline{E}_t + \operatorname{div}\left(\left(E + p + \frac{1}{2}\left|\overline{\mathbf{B}}\right|^2\right)\mathbf{u} - (\mathbf{u}\cdot\overline{\mathbf{B}})\overline{\mathbf{B}}\right) &= -(\mathbf{u}\cdot\overline{\mathbf{B}})(\operatorname{div}\overline{\mathbf{B}}) - \rho g\,(\mathbf{u}\cdot\mathbf{e}_3)\,.
\end{aligned}
\tag{2.1}
$$

The system is coupled with an ideal gas equation of state (1.2) and all the quantities in (2.1) are as defined before. The difference between the standard form (1.1) and (2.1) lies in the source term that is proportional to the divergence of the magnetic field. However, applying the divergence operator to both sides of (2.1), we obtain

$$
(\operatorname{div}\overline{\mathbf{B}})_t + \operatorname{div}\left(\mathbf{u}\left(\operatorname{div}\overline{\mathbf{B}}\right)\right) = 0. \tag{2.2}
$$

Hence, initial divergence free fields remain divergence free under time evolution in (2.1) showing that the two forms are equivalent. Furthermore, the Godunov-Powell system is Galilean invariant ([45]) and symmetrizable ([23]). Hence, we discretize the Godunov-Powell form (2.1) instead of the standard form (1.1).

Since we are interested in dynamics near the steady states (1.6) and (1.8), we consider a further modification of the system (2.1). Assume that there exists a magnetic field $\widetilde{\mathbf{B}}$ satisfying the following assumptions,

$$\widetilde{\mathbf{B}}_t = 0, \quad \operatorname{div}(\widetilde{\mathbf{B}}) = 0, \text{ and } \operatorname{curl}(\widetilde{\mathbf{B}}) = 0. \tag{2.3}$$

Specific examples of such *potential* magnetic fields will be given in the sequel. We define deviations $\mathbf{B}$ of this potential field $\widetilde{\mathbf{B}}$ by,

$$\mathbf{B} = \overline{\mathbf{B}} - \widetilde{\mathbf{B}}.$$

We substitute the above form in (2.1) and after some calculations (see [45]), we obtain the following modified system,

$$\begin{aligned}
&\rho_t + \operatorname{div}(\rho\mathbf{u}) = 0,\\
&(\rho\mathbf{u})_t + \operatorname{div}\left(\rho\mathbf{u}\otimes\mathbf{u} + \left(p + \frac{1}{2}|\mathbf{B}|^2 + \widetilde{\mathbf{B}}\cdot\mathbf{B}\right) I - \mathbf{B}\otimes\mathbf{B} - \widetilde{\mathbf{B}}\otimes\mathbf{B} - \mathbf{B}\otimes\widetilde{\mathbf{B}}\right)\\
&\qquad\qquad = -\left(\mathbf{B} + \widetilde{\mathbf{B}}\right)(\operatorname{div}\mathbf{B}) - \rho g\mathbf{e}_3,\\
&\mathbf{B}_t + \operatorname{div}\left(\mathbf{u}\otimes\mathbf{B} - \mathbf{B}\otimes\mathbf{u} + \mathbf{u}\otimes\widetilde{\mathbf{B}} - \widetilde{\mathbf{B}}\otimes\mathbf{u}\right) = -\mathbf{u}(\operatorname{div}\mathbf{B}),\\
&E_t + \operatorname{div}\left(\left(E + p + \frac{1}{2}|\mathbf{B}|^2 + \mathbf{B}\cdot\widetilde{\mathbf{B}}\right)\mathbf{u} - (\mathbf{u}\cdot\mathbf{B})\mathbf{B} - \left(\mathbf{u}\cdot\widetilde{\mathbf{B}}\right)\mathbf{B}\right)\\
&\qquad\qquad = -(\mathbf{u}\cdot\mathbf{B})(\operatorname{div}\mathbf{B}) - \rho g\left(\mathbf{u}\cdot\mathbf{e}_3\right),
\end{aligned} \tag{2.4}$$

where $E = \frac{p}{\gamma-1} + \frac{1}{2}|\mathbf{B}|^2 + \frac{1}{2}\rho|\mathbf{u}|^2$. The variable of interest is now the magnetic field deviation $\mathbf{B}$, and the background magnetic field $\widetilde{\mathbf{B}}$ satisfying (2.3) appears as a coefficient in the above equations.

Remark 2.1. The only assumptions used in deriving (2.4) are given by (2.3). In particular, no linearization assumptions were made nor was any condition imposed on the magnitude of $\mathbf{B}$. Hence, the above equations (2.4) can be thought of as an equivalent form of the MHD equations with gravity (1.1).

Writing (2.4) as a balance law explicitly, we obtain,

$$\mathbf{U}_t + (\mathbf{f}(\mathbf{U},\widetilde{\mathbf{B}})_x + \mathbf{g}(\mathbf{U},\widetilde{\mathbf{B}})_y + \mathbf{h}(\mathbf{U},\widetilde{\mathbf{B}})_z = \mathbf{s}^1(\mathbf{U},\widetilde{\mathbf{B}}) + \mathbf{s}^2(\mathbf{U},\widetilde{\mathbf{B}}) + +\mathbf{s}^3(\mathbf{U},\widetilde{\mathbf{B}}) + \mathbf{s}^g(\mathbf{U}), \tag{2.5}$$

where

$$\mathbf{U} = \{\rho, \rho u_1, \rho u_2, \rho u_3, B_1, B_2, B_3, E\}$$

is the vector of conserved variables and $\widetilde{\mathbf{B}} = \{\widetilde{B}_1, \widetilde{B}_2, \widetilde{B}_3\}$ is any background magnetic field defined by (2.4). The above form clearly illustrates that the fluxes and the Godunov-Powell source term depend on the coefficient $\widetilde{\mathbf{B}}$. Hence, (2.5) is an example of a balance law with spatially varying coefficients. Such equations have many

interesting properties (see [39]) for a detailed exposition). The fluxes and sources in (2.5) are given by (2.6)

$$\mathbf{f} = \begin{pmatrix} \rho u_1 \\ \rho u_1^2 + \pi_1 - \frac{B_1^2}{2} - \widetilde{B}_1 B_1 \\ \rho u_1 u_2 - B_1 B_2 - \widetilde{B}_1 B_2 - B_1 \widetilde{B}_2 \\ \rho u_1 u_3 - B_1 B_3 - \widetilde{B}_1 B_3 - B_1 \widetilde{B}_3 \\ 0 \\ u_1 \left(B_2 + \widetilde{B}_2\right) - u_2 \left(B_1 + \widetilde{B}_1\right) \\ u_1 \left(B_3 + \widetilde{B}_3\right) - u_3 \left(B_3 + \widetilde{B}_3\right) \\ (E + \pi_1) u_1 - u_1 \frac{B_1^2}{2} - \left(B_1 + \widetilde{B}_1\right)(u_2 B_2 + u_3 B_3) \end{pmatrix}, \quad \mathbf{s}^1 = \begin{pmatrix} 0, \\ -\left(\frac{B_1^2}{2}\right)_x - \widetilde{B}_1 (B_1)_x \\ -\left(B_2 + \widetilde{B}_2\right)(B_1)_x \\ -\left(B_3 + \widetilde{B}_3\right)(B_1)_x \\ -u_1 (B_1)_x \\ -u_2 (B_1)_x \\ -u_3 (B_1)_x \\ -u_1 \left(\frac{B_1^2}{2}\right)_x - (u_2 B_2 + u_3 B_3)(B_1)_x \end{pmatrix},$$

$$\mathbf{g} = \begin{pmatrix} \rho u_2 \\ \rho u_1 u_2 - B_1 B_2 - \widetilde{B}_1 B_2 - B_1 \widetilde{B}_2 \\ \rho u_2^2 + \pi_2 - \frac{B_2^2}{2} - \widetilde{B}_2 B_2 \\ \rho u_2 u_3 - B_2 B_3 - \widetilde{B}_2 B_3 - B_2 \widetilde{B}_3 \\ u_2 \left(B_2 + \widetilde{B}_2\right) - u_2 \left(B_2 + \widetilde{B}_2\right) \\ 0 \\ u_2 \left(B_3 + \widetilde{B}_3\right) - u_3 \left(B_3 + \widetilde{B}_3\right) \\ (E + \pi_2) u_2 - u_2 \frac{B_2^2}{2} - \left(B_2 + \widetilde{B}_2\right)(u_2 B_2 + u_3 B_3) \end{pmatrix}, \quad \mathbf{s}^2 = \begin{pmatrix} 0, \\ -\left(B_1 + \widetilde{B}_1\right)(B_2)_y \\ -\left(\frac{B_2^2}{2}\right)_y - \widetilde{B}_2 (B_2)_y \\ -\left(B_3 + \widetilde{B}_3\right)(B_2)_y \\ -u_1 (B_2)_y \\ -u_2 (B_2)_y \\ -u_3 (B_2)_y \\ -u_2 \left(\frac{B_2^2}{2}\right)_y - (u_1 B_1 + u_3 B_3)(B_2)_y \end{pmatrix}$$

$$\mathbf{h} = \begin{pmatrix} \rho u_3 \\ \rho u_1 u_3 - B_1 B_3 - \widetilde{B}_1 B_3 - B_1 \widetilde{B}_3 \\ \rho u_2 u_3 - B_2 B_3 - \widetilde{B}_2 B_3 - B_2 \widetilde{B}_3 \\ \rho u_3^2 + \pi_3 - \frac{B_3^2}{2} - \widetilde{B}_3 B_3 \\ u_3 \left(B_1 + \widetilde{B}_1\right) - u_3 \left(B_1 + \widetilde{B}_1\right) \\ u_3 \left(B_2 + \widetilde{B}_2\right) - u_3 \left(B_2 + \widetilde{B}_2\right) \\ (E + \pi_3) u_3 - u_3 \frac{B_3^2}{2} - \left(B_3 + \widetilde{B}_3\right)(u_1 B_1 + u_2 B_2) \end{pmatrix}, \quad \mathbf{s}^3 = \begin{pmatrix} 0, \\ -\left(B_1 + \widetilde{B}_1\right)(B_3)_z \\ -\left(B_2 + \widetilde{B}_2\right)(B_3)_z \\ -\left(\frac{B_3^2}{2}\right)_z - \widetilde{B}_3 (B_3) \\ -u_1 (B_3)_z \\ -u_2 (B_3)_z \\ -u_3 (B_3)_z \\ -u_3 \left(\frac{B_3^2}{2}\right)_z - (u_1 B_1 + u_2 B_2)(B_3)_z, \end{pmatrix}$$

where we have defined,

$$\begin{aligned} &\pi_1 = p + \frac{B_2^2 + B_3^2}{2} + B_2 \widetilde{B}_2 + B_3 \widetilde{B}_3, \quad \pi_2 = p + \frac{B_1^2 + B_3^2}{2} + B_1 \widetilde{B}_1 + B_3 \widetilde{B}_3, \\ &\pi_3 = p + \frac{B_1^2 + B_2^2}{2} + B_1 \widetilde{B}_1 + B_2 \widetilde{B}_2. \end{aligned} \tag{2.7}$$

Finally, the gravitational source term is given by

$$\mathbf{s}^g = \{0, 0, -\rho g, 0, 0, 0, 0, -\rho u_3\ g\}. \tag{2.8}$$

Considering the primitive variables $\mathbf{V} = \{\rho, \mathbf{u}, \mathbf{B}, p\}$, we can write (2.5) in the quasilinear form

$$\mathbf{V}_t + A\mathbf{V}_x + B\mathbf{V}_y + C\mathbf{V}_z = \widetilde{\mathbf{S}},$$

where $(A, B, C) = (\partial_{\mathbf{U}}\mathbf{f}, \partial_{\mathbf{U}}\mathbf{g}, \partial_{\mathbf{U}}\mathbf{h})$ are the flux Jacobians. Denoting the sound speed $a^2 = \frac{\gamma p}{\rho}$ and $b_{1,2,3} = \frac{\overline{\mathbf{B}}_{1,2,3}}{\sqrt{\rho}}$, $b^2 = b_1^2 + b_2^2 + b_3^2$, the eigenvalues of A are calculated (see [45]) as

$$\begin{aligned} &\lambda_1 = u_1 - c_f, \quad \lambda_2 = u_1 - b_1, \quad \lambda_3 = u_1 - c_s, \quad \lambda_4 = u_1, \\ &\lambda_5 = u_1, \quad \lambda_6 = u_1 + c_s, \quad \lambda_7 = u_1 + b_1, \quad \lambda_8 = u_1 + c_f, \end{aligned} \tag{2.9}$$

where c_f, c_s are given by

$$c_f^2 = \frac{1}{2}\left(a^2+b^2+\sqrt{(a^2+b^2)^2-4a^2b_1^2}\right), \quad c_s^2 = \frac{1}{2}\left(a^2+b^2-\sqrt{(a^2+b^2)^2-4a^2b_1^2}\right).$$

The waves corresponding to λ_1, λ_8 are termed as fast waves, ones corresponding to λ_3, λ_6 as slow waves, those corresponding to λ_2, λ_7 as Alfvén waves and the wave associated with $\lambda_{4,5}$ is a contact or shear wave. Note that the coefficient $\widetilde{\mathbf{B}}$ enters into the expressions for the eigenvalues. The eigenvalues of B and C are analogously defined.

2.1. **Characterization of steady states.** In terms of the system (2.4), the hydrodynamic steady state (1.6) leads to a zero embedded magnetic field,

$$\widetilde{\mathbf{B}} \equiv 0. \tag{2.10}$$

2.1.1. *Magnetic steady states.* Non-trivial solutions of (2.3) lead to interesting magnetic steady states. Note that solutions of (2.3) can be characterized by vector harmonic functions. In three space dimensions, a Fourier solution of (2.3) can be written down explicitly as,

$$\begin{aligned}
\widetilde{B}_1(x,y,z) &= \sum_{l=1}^{L}\sum_{m=0}^{M} \frac{l\ \alpha_{lm}}{\sqrt{l^2+m^2}} e^{-2\pi\sqrt{l^2+m^2}z}\Big(\quad a_{lm}\sin(2\pi lx)\cos(2\pi my) - b_{lm}\cos(2\pi lx)\sin(2\pi my) \\
&\qquad\qquad - c_{lm}\cos(2\pi lx)\cos(2\pi my) + d_{lm}\sin(2\pi lx)\sin(2\pi my)\Big), \\
\widetilde{B}_2(x,y,z) &= \sum_{l=0}^{L}\sum_{m=1}^{M} \frac{m\ \alpha_{lm}}{\sqrt{l^2+m^2}} e^{-2\pi\sqrt{l^2+m^2}z}\Big(\quad a_{lm}\cos(2\pi lx)\sin(2\pi my) - b_{lm}\sin(2\pi lx)\cos(2\pi my) \\
&\qquad\qquad + c_{lm}\sin(2\pi lx)\sin(2\pi my) - d_{lm}\cos(2\pi lx)\cos(2\pi my)\Big), \\
\widetilde{B}_3(x,y,z) &= \sum_{l=0}^{L}\sum_{m=0}^{M} \alpha_{lm} e^{-2\pi\sqrt{l^2+m^2}z}\Big(\quad a_{lm}\cos(2\pi lx)\cos(2\pi my) + b_{lm}\sin(2\pi lx)\sin(2\pi my) \\
&\qquad\qquad + c_{lm}\sin(2\pi lx)\cos(2\pi my) + d_{lm}\cos(2\pi lx)\sin(2\pi my)\Big),
\end{aligned} \tag{2.11}$$

where $a_{lm}, b_{lm}, c_{lm}, d_{lm}$ are the Fourier co-efficients corresponding to the background magnetic field $\widetilde{B}_3(x,y,0)$ at the bottom of the domain, and L, M are the maximum number of modes for the indices l and m respectively. The factor α_{lm} is $1/4$ if $l = m = 0$, $1/2$ if l or m is zero, and 1 otherwise. It can be readily checked that (2.11) satisfies (2.3). See also [20, 22] for a two dimensional version.

In all the cases, the steady state is given by

$$\mathbf{u} \equiv \mathbf{0}, \quad \mathbf{B} \equiv 0 \quad \rho(z) = \frac{\rho_0 T_0}{T(z)} e^{-\frac{\alpha(z)}{H}}, \quad p(z) = p_0 e^{-\frac{\alpha(z)}{H}}. \tag{2.12}$$

Hence, the only difference lies in the choice of the background magnetic field $\widetilde{B}$. This formulation allows us to treat a wide array of steady states within a unified framework.

3. Numerical Schemes

For simplicity, we approximate (2.5) in a Cartesian domain $\mathbf{x} = (x,y,z) \in [X_l, X_r] \times [Y_l, Y_r] \times [Z_b, Z_t]$ and discretize it by a uniform grid in all directions with the grid spacing $\Delta x, \Delta y$ and Δz. We set $x_i = X_l + i\Delta x$, $y_j = Y_l + j\Delta y$ and $z_k = Z_b + k\Delta z$. The indices are $0 \le i \le N_x$, $0 \le j \le N_y$ and $0 \le k \le N_z$. Set $x_{i+1/2} = x_i + \Delta x/2$, $y_{j+1/2} = y_j + \Delta y/2$ and $z_{k+1/2} = z_k + \Delta z/2$, and let $\mathcal{C}_{i,j,k} = [x_{i-1/2}, x_{i+1/2}) \times [y_{j-1/2}, y_{j+1/2}) \times [z_{k-1/2}, z_{k+1/2})$ denote a typical cell. The cell average of the unknown state vector $\mathbf{W}$ (approximating $\mathbf{U}$) over $\mathcal{C}_{i,j,k}$ at time t^n is denoted $\mathbf{W}^n_{i,j,k}$.

3.1. **First order schemes.** A standard finite volume scheme (first-order in both space and time) (see [32]) is obtained by integrating the balance law (2.5) over the cell $\mathcal{C}_{i,j,k}$ and the time interval $[t^n, t^{n+1})$ with $t^{n+1} = t^n + \Delta t^n$, where the time-step Δt^n is determined by a suitable CFL condition. The resulting fully-discrete form of the scheme is

$$\begin{aligned}\mathbf{W}_{i,j,k}^{n+1} = \mathbf{W}_{i,j,k}^{n} &- \frac{\Delta t^n}{\Delta x}(\mathbf{F}_{i+1/2,j,k}^{n} - \mathbf{F}_{i-1/2,j,k}^{n}) - \frac{\Delta t^n}{\Delta y}(\mathbf{G}_{i,j+1/2,k}^{n} - \mathbf{G}_{i,j-1/2,k}^{n}) \\ &- \frac{\Delta t^n}{\Delta z}(\mathbf{H}_{i,j,k+1/2}^{n} - \mathbf{H}_{i,j,k-1/2}^{n}) + \Delta t^n(\mathbf{S}_{i,j,k}^{1,n} + \mathbf{S}_{i,j,k}^{2,n} + +\mathbf{S}_{i,j,k}^{3,n} + \mathbf{S}_{i,j,k}^{g,n}).\end{aligned} \tag{3.1}$$

The numerical fluxes $\mathbf{F}$, $\mathbf{G}$, $\mathbf{H}$ and discretized sources $\mathbf{S}^1$, $\mathbf{S}^2$, $\mathbf{S}^3$ and $\mathbf{S}^g$ are specified in the following sections

3.1.1. *Numerical flux and Godunov-Powell source in the x-direction.* Following [21, 22], we determine the numerical flux $\mathbf{F}_{i+1/2,j}^{n}$ and the source term $\mathbf{S}_{i,j}^{1,n}$ from the (approximate) solution of the following Riemann problem

$$\mathbf{W}_t + \mathbf{f}\left(\mathbf{W}, \widetilde{\mathbf{B}}_M\right)_x = \mathbf{s}^1\left(\mathbf{W}, \widetilde{\mathbf{B}}_M, \mathbf{W}_x\right), \quad \mathbf{W}(x,0) = \begin{cases}\mathbf{W}_L & x < 0, \\ \mathbf{W}_R & x > 0,\end{cases} \tag{3.2}$$

where $\mathbf{f}$ and $\mathbf{s}^1$ are defined in (2.6). The coefficient $\widetilde{\mathbf{B}}_M$ in (3.2) is given by the average,

$$\widetilde{\mathbf{B}}_M = \widetilde{\mathbf{B}}_{i+1/2,j} = \frac{\widetilde{\mathbf{B}}_{i,j} + \widetilde{\mathbf{B}}_{i+1,j}}{2}. \tag{3.3}$$

Hence, we stagger the coefficient $\widetilde{\mathbf{B}}$ in defining the approximate Riemann solver. This approach is a popular discretization of balance laws with coefficients ([28]) and results in a simplification of the Riemann problem.

3.1.2. *The HLL three wave solver.* There are eight possible waves in the exact solution of the Riemann problem (3.2). We will approximate these eight waves with three waves, i.e, two representing the outermost fast waves and a middle wave approximating the material contact discontinuity. This approximate solution and fluxes for (3.2) are given by

$$\mathbf{W}^{H_3} = \begin{cases}\mathbf{W}_L & \text{if } \frac{x}{t} \le s_L, \\ \mathbf{W}_L^* & \text{if } s_L < \frac{x}{t} < s_M, \\ \mathbf{W}_R^* & \text{if } s_M < \frac{x}{t} < s_R, \\ \mathbf{W}_R & \text{if } s_R \le \frac{x}{t}, \end{cases} \qquad \mathbf{F}^{H_3}\left(\mathbf{W}_L, \mathbf{W}_R, \widetilde{\mathbf{B}}_M\right) = \begin{cases}\mathbf{F}_L & \text{if } \frac{x}{t} \le s_L, \\ \mathbf{F}_L^* & \text{if } s_L < \frac{x}{t} < s_M, \\ \mathbf{F}_R^* & \text{if } s_M < \frac{x}{t} < s_R, \\ \mathbf{F}_R & \text{if } s_R \le \frac{x}{t}. \end{cases} \tag{3.4}$$

The outer wave speeds s_L and s_R model the fast magneto-sonic waves and are defined as in [24, 16], i.e.,

$$s_L = \min\left\{u_{1L} - c_{fL},\ \overline{u}_1 - \overline{c}_f\right\}, \quad s_R = \max\left\{u_{1R} + c_{fR},\ \overline{u}_1 + \overline{c}_f\right\}, \tag{3.5}$$

where $\overline{u}_1$ and $\overline{c}_f$ are the normal velocity and the fast wave speed of the Jacobian matrix $A((\mathbf{W}_L + \mathbf{W}_R)/2)$ respectively. This choice is important for numerical stability and accuracy.

In order to describe the solver, we need to prescribe the speed of the middle wave s_M and the intermediate states $\mathbf{W}_L^*, \mathbf{W}_R^*$. The middle wave models a material contact discontinuity. Hence, the velocity field and the tangential magnetic fields are assumed to be constant across the middle wave. This allows us to define $\mathbf{u}^* = \mathbf{u}_L^* = \mathbf{u}_R^*$, $B_2^* = B_{2L}^* = B_{2R}^*$ and $B_3^* = B_{3L}^* = B_{3R}^*$. As in [21, 22], the normal magnetic field B_1 is not assumed to be constant but jumps only across the middle wave (modeling the linear degenerate "divergence wave" implied by (2.2)). The intermediate states are determined by local conservation. Local conservation across the outermost waves means that

$$s_L\mathbf{W}_L^* - \mathbf{F}_L^* = s_L\mathbf{W}_L - \mathbf{F}_L, \text{ and } s_R\mathbf{W}_R - \mathbf{F}_R = s_R\mathbf{W}_R^* - \mathbf{F}_R^*. \tag{3.6}$$

Conservation across the middle wave s_M involves taking the source term $\mathbf{s}^1$ in (3.2) into account. The conservation relation reads

$$s_M\mathbf{W}_R^* - s_M\mathbf{W}_L^* = \mathbf{F}_R^* - \mathbf{F}_L^* + \mathbf{s}^{1,*} \tag{3.7}$$

where

$$\mathbf{s}^{1,*} = \begin{pmatrix} 0 \\ -\frac{B_{1R}^2 - B_{1L}^2}{2} - \widetilde{B}_{1M}\left(B_{1R} - B_{1L}\right) \\ -\left(B_2^* + \widetilde{B}_{2M}\right)\left(B_{1R} - B_{1L}\right) \\ -\left(B_3^* + \widetilde{B}_{3M}\right)\left(B_{1R} - B_{1L}\right) \\ -\mathbf{u}^*\left(B_{1R} - B_{1L}\right) \\ -u_1^* \frac{B_{1R}^2 - B_{1L}^2}{2} - \left(u_2^* B_2^* + u_3^* B_3^*\right)\left(B_{1R} - B_{1L}\right) \end{pmatrix}. \tag{3.8}$$

The above expression follows from the assumption that B_1 jumps only across the middle wave while the velocity field and the tangential components of the magnetic field remain constant.

Applying the conservation relations (3.6) and (3.7), we obtain (check [22], section 3.1.2 for details) the following intermediate states,

$$\begin{aligned}
\rho_\theta^* &= \rho_\theta \frac{u_{1\theta} - s_\theta}{s_M - s_\theta}, \quad \theta \in \{L, R\}, \\
s_M = u_1^* &= \frac{\pi_{1R} - \pi_{1L} + \rho_R u_{1R}(u_{1R} - s_R) - \rho_L u_{1L}(u_{1L} - s_L)}{\rho_R(u_{1R} - s_R) - \rho_L(u_{1L} - s_L)}, \\
\pi_{1\theta}^* &= \pi_{1\theta} + \rho_\theta(u_{1\theta} - s_\theta)(u_{1\theta} - s_M), \quad \theta \in \{L, R\}, \\
u_\sigma^* &= \frac{\zeta c_\sigma - \xi d_\sigma}{\alpha\zeta + \xi^2}, \quad \sigma \in \{2, 3\} \\
B_\sigma^* &= \frac{-\alpha d_\sigma - \xi c_\sigma}{\alpha\zeta + \xi^2}, \quad \sigma \in \{2, 3\}, \\
E_\theta^* &= \frac{1}{s_M - s_\theta}\Big(E_\theta\left(u_{1\theta} - s_\theta\right) + \pi_{1\theta} u_{1\theta} - \pi_{1\theta}^* s_M + \frac{B_{1\theta}^2}{2}\left(u_{1\theta} - s_M\right) \\
&\quad + \left(B_{1\theta} + \widetilde{B}_{1M}\right)\left(B_{2\theta} u_{2\theta} + B_{3\theta} u_{3\theta} - B_{2\theta}^* u_{2\theta}^* - B_{3\theta}^* u_{3\theta}^*\right)\Big), \quad \theta \in \{L, R\},
\end{aligned} \tag{3.9}$$

where

$$\begin{aligned}
c_\sigma &= \rho_R u_{\sigma R}\left(u_{1R} - s_R\right) - \rho_L u_{\sigma L}\left(u_{1L} - s_L\right) - \left(B_{1R} B_{\sigma R} - B_{1L} B_{\sigma L}\right) - \widetilde{B}_{1M}\left(B_{\sigma R} - B_{\sigma L}\right), \\
d_\sigma &= B_{\sigma R}\left(u_{1R} - s_R\right) - B_{\sigma L}\left(u_{1L} - s_L\right) - \left(B_{1L} u_{\sigma L} - B_{1R} u_{\sigma R}\right) + \widetilde{B}_{\sigma M}\left(u_{1R} - u_{1L}\right) - \widetilde{B}_1\left(u_{\sigma R} - u_{\sigma L}\right), \\
\alpha &= \rho_R\left(u_{1R} - s_R\right) - \rho_L\left(u_{1L} - s_L\right), \quad \zeta = s_R - s_L, \quad \xi = B_{1R} - B_{1L}.
\end{aligned} \tag{3.10}$$

The denominator $\alpha\zeta + \xi^2$ in (3.9) may become zero in some cases leading to degenerate states. This can easily be avoided by widening the wave fan slightly. The recipe is prescribed in [22], remark 3.1.

The intermediate fluxes are obtained in terms of the intermediate states by local conservation (3.6),

$$\mathbf{F}_L^* = \mathbf{F}_L + s_L(\mathbf{W}_L^* - \mathbf{W}_L), \quad \mathbf{F}_R^* = \mathbf{F}_R + s_R(\mathbf{W}_R^* - \mathbf{W}_R).$$

Note that $\mathbf{F}_{L/R}^*$ may differ from $\mathbf{F}(\mathbf{W}_{L/R}^*)$. Combining the above expressions for the states and the fluxes, we write down our explicit flux formula for the three-wave solver as

$$\mathbf{F}_{i+1/2,j,k}^{H_3} = \begin{cases} \mathbf{F}_{i,j,k} & , \text{ if } (s_L)_{i+1/2,j,k} > 0, \\ \mathbf{F}_{i,j,k}^* & , \text{ if } (s_L)_{i+1/2,j,k} \le 0 \wedge (s_M)_{i+1/2,j,k} \ge 0, \\ \mathbf{F}_{i+1,j,k}^* & , \text{ if } (s_M)_{i+1/2,j,k} < 0 \wedge (s_R)_{i+1/2,j,k} \ge 0, \\ \mathbf{F}_{i+1,j,k} & , \text{ if } (s_R)_{i+1/2,j,k} < 0. \end{cases} \tag{3.11}$$

while the discrete source $\mathbf{S}^1$ takes the form

$$\mathbf{S}_{i,j,k}^{1,n} = \mathbf{s}_{i-1/2,j,k}^{1,*} \mathbf{1}_{\{(s_{M,i-1/2,j,k} \ge 0)\}} + \mathbf{s}_{i+1/2,j,k}^{1,*} \mathbf{1}_{\{(s_{M,i+1/2,j,k} < 0)\}}, \tag{3.12}$$

where $\mathbf{s}_{i\pm1/2,j,k}^{1,*}$ is defined in analogy to (3.8).

We emphasize that the discrete Godunov-Powell source term in each cell is naturally derived from Riemann solutions at the bordering interfaces and depends on the sign of the middle wave at each interface. Thus, the

Godunov-Powell source term is suitably *upwinded*. Note that assuming the normal magnetic field B_1 to be constant for the whole domain leads to the source term being zero. This approach follows [21],[8],[22] and is very different from the usual centered discretization of the Godunov-Powell source term ([45] and references therein).

Remark 3.1. The above fluxes and sources are designed using a three wave solver. An alternative would be to design a five wave solver like in [40],[21]. This solver models Alfvén waves in addition to the fast waves and the contact discontinuity. We can follow the steps of [20] to design a five wave solver for (3.2).

3.1.3. *Fluxes and sources in the y-direction.* The numerical flux $\mathbf{G}$ and discrete Godunov-Powell source term $\mathbf{S}^2$ in (3.1) are similarly described in terms of the following Riemann problem

$$\mathbf{W}_t + \mathbf{g}(\mathbf{W}, \widetilde{\mathbf{B}}_M)_y = \mathbf{s}^2(\mathbf{W}, \widetilde{\mathbf{B}}_M, \mathbf{W}_y), \quad \mathbf{W}(y,0) = \begin{cases} \mathbf{W}_L & y < 0, \\ \mathbf{W}_R & y > 0, \end{cases} \tag{3.13}$$

where $\mathbf{g}$ and $\mathbf{s}^2$ are defined in (2.6). We substitute

$$\mathbf{W}_L = \mathbf{W}_{i,j,k}, \quad \mathbf{W}_R = \mathbf{W}_{i,j+1,k}, \quad \widetilde{\mathbf{B}}_M = \frac{\widetilde{\mathbf{B}}_{i,j} + \widetilde{\mathbf{B}}_{i,j+1}}{2}$$

and obtain the numerical flux $\mathbf{G}_{i,j+1/2,k}$ and discrete Godunov-Powell source $\mathbf{S}^2_{i,j,k}$ analogously to the procedure outlined in the previous section for obtaining the numerical flux and source in the x-direction.

3.1.4. *Fluxes and sources in the z-direction.* The numerical flux $\mathbf{H}$ and discrete Godunov-Powell source term $\mathbf{S}^3$ in (3.1) are similarly described in terms of the following Riemann problem

$$\mathbf{W}_t + \mathbf{h}(\mathbf{W}, \widetilde{\mathbf{B}}_M)_z = \mathbf{s}^3(\mathbf{W}, \widetilde{\mathbf{B}}_M, \mathbf{W}_z), \quad \mathbf{W}(y,0) = \begin{cases} \mathbf{W}_T & y < 0, \\ \mathbf{W}_B & y > 0, \end{cases} \tag{3.14}$$

where $\mathbf{h}$ and $\mathbf{s}^3$ are defined in (2.6). The straight forward way to specify initial data $\mathbf{W}_{T,B}$ in the above problem is to use the states $\mathbf{W}_B = \mathbf{W}^n_{i,j,k}$ and $\mathbf{W}_T = \mathbf{W}^n_{i,j,k+1}$. However, this approach leads to a scheme that does not preserve discrete versions of the interesting steady states (1.6) and (1.8). Therefore we must design suitable fluxes in order to design well-balanced schemes.

3.1.5. *Local Hydrostatic pressure reconstructions.* Instead of just using the cell averages below and above the interface as data in (3.14), we perform a local hydrostatic reconstruction of the pressure inside the cell by utilizing the special structure of the steady states (1.6),(1.8), i.e., we observe that the pressure at steady state (1.6) and (1.8) has an exponentially decaying profile that is scaled in terms of the function α (1.5). We will use the same structure locally inside a cell to define the vector of primitive variables,

$$\mathbf{V}_B = \{\rho^n_{i.j,k}, \mathbf{u}^n_{i,j,k}, \mathbf{B}^n_{i,j,k}, p^{n,-}_{i,j,k+1/2}\}, \quad \mathbf{V}_T = \{\rho^n_{i,j,k+1}, \mathbf{u}^n_{i,j,k+1}, \mathbf{B}^n_{i,j,k+1}, p^{n,+}_{i,j+1/2}\}, \tag{3.15}$$

where the reconstructed pressure is given in terms of extrapolated cell averages by first defining the local temperature,

$$T^n_{i,j,k} = \frac{p^n_{i,j,k}}{gH\rho^n_{i,j,k}}. \tag{3.16}$$

The piecewise constant temperature defines the scaling function α by (1.5). We can compute the differences in α and use it to define the reconstructed local pressure,

$$p^{n,-}_{i,j,k+1/2} = p^n_{i,j,k} e^{\frac{-\Delta z}{2HT^n_{i,j,k}}}, \quad p^{n,+}_{i,j,k+1/2} = p^n_{i,j,k+1} e^{\frac{\Delta z}{2HT^n_{i,j,k+1}}}, \tag{3.17}$$

The above sub-cell hydrostatic reconstruction is similar to the one proposed in [22]. Note that the local reconstructed pressures $p^{n,\pm}_{i,j,k+1/2}$ (3.17) are inspired by the form of the steady state pressure in (1.6) and (1.8), and will be shown to lead to a *well-balanced* scheme in the sequel.

The data $\mathbf{W}_B$ and $\mathbf{W}_T$ (in terms of conservative variables) are easily obtained from the primitive variables $\mathbf{V}_B$, $\mathbf{V}_T$. The coefficient $\widetilde{\mathbf{B}}_M$ in (3.14) is given by the average,

$$\widetilde{\mathbf{B}}_M = \widetilde{\mathbf{B}}_{i,j,k+1/2} = \frac{\widetilde{\mathbf{B}}_{i,j,k} + \widetilde{\mathbf{B}}_{i,j,k+1}}{2}. \tag{3.18}$$

Hence, we stagger the coefficient $\widetilde{\mathbf{B}}$ in defining the approximate Riemann solver as in the other directions.

An approximate Riemann solution of the problem (3.2) in terms of the HLL three wave solver of the previous section is easily obtained by repeating the approach of describing the solver in the x- and y-direction. This can be used to describe the flux $\mathbf{H}$ and source $\mathbf{S}^3$. Note that the difference between the design of the fluxes and Godunov-Powell sources in the x, y- and the z-directions is due to the use of local hydrostatic reconstructions of the pressure in the z-direction. We remark that although the steady state density has a scaled exponential profile, we will not be reconstructing it locally as it is not necessary for well-balancing (In [22] where the local hydrostatic density was also reconstructed).

We need the following useful lemma in the sequel,

Lemma 3.1. *We denote the numerical flux (in the z-direction) defined by the HLL three wave solver as*

$$\mathbf{H}_{i,j,k+1/2} = \mathbf{H}\left(\rho_{i,j,k}, \mathbf{u}_{i,j,k}, \mathbf{B}_{i,j,k}, p^-_{i,j,k+1/2}, \rho_{i,j,k+1}, \mathbf{u}_{i,j,k+1}, \mathbf{B}_{i,j,k+1}, p^+_{i,j,k+1/2}, \widetilde{\mathbf{B}}_{i,j,k+1/2}\right).$$

If we have,

$$\begin{aligned} p^-_{i,j,k+1.2} = p^+_{i,j,k+1/2} = p_{i,j,k+1/2}, \\ (\mathbf{u}_{i,j,k}, \mathbf{B}_{i,j,k}) = (\mathbf{u}_{i,j,k+1}, \mathbf{B}_{i,j,k+1}) = (\mathbf{0}, \mathbf{0}), \end{aligned} \tag{3.19}$$

then the numerical flux is given by,

$$\begin{aligned} \mathbf{H}_{i,j,k+1/2} &= \mathbf{H}\left(\rho_{i,j,k}, \mathbf{0}, \mathbf{0}, p_{i,j,k+1/2}, \rho_{i,j,k+1}, \mathbf{0}, \mathbf{0}, p_{i,j,k+1/2}, \widetilde{\mathbf{B}}_{i,j,k+1/2}\right) \\ &= \left\{0, 0, 0, p_{i,j,k+1/2}, 0, 0, 0, 0\right\}, \end{aligned} \tag{3.20}$$

where $\mathbf{0} = (0, 0, 0)$.

The proof of this lemma lies in checking (3.20) in a straightforward manner when the adjacent states in (3.14) satisfy (3.19) by plugging in (3.19) in expressions analogous to (3.9). The interpretation of the lemma is that our approximate Riemann solver exactly resolves stationary material contact discontinuities. We need this property to prove well-balancing. Since e.g. two-wave HLL solvers diffuse stationary contacts, they will not suffice for our purpose.

3.1.6. *Discretization of the gravitational source term.* We need to discretize the gravity source term to define $\mathbf{S}^g$ in (3.1). Instead of using a simple evaluation of the gravity term (it does not involve any derivatives) inside each cell, we follow an approach suggested in [1] for shallow water equations with topography and [22] for stratified MHD to define

$$\mathbf{S}^{g,n}_{i,j,k} = \left\{0, 0, \frac{p^{n,-}_{i,j,k+1/2} - p^{n,+}_{i,j,k-1/2}}{\Delta z}, 0, 0, 0, 0, -\rho^n_{i,j,k}(u^n_3)_{i,j,k}\ g\right\}. \tag{3.21}$$

where $p^{n,-}_{i,j,k+1/2}, p^{n,+}_{i,j,k-1/2}$ are defined in (3.17). We will prove that this discretization of the gravity source term is consistent, and that it ensures well-balancing of the scheme.

3.1.7. *Boundary conditions:* In order to complete our description of the scheme (3.1), we need to specify boundary conditions in all directions. As mentioned before, we use periodic boundary conditions in the horizontal directions by setting,

$$\mathbf{W}^n_{0,j,k} = \mathbf{W}^n_{N_x,j,k}, \quad \mathbf{W}^n_{N_x+1,j,k} = \mathbf{W}^n_{1,j,k}, \quad \mathbf{W}^n_{i,0,k} = \mathbf{W}^n_{i,N_y,k}, \quad \mathbf{W}^n_{i,N_y+1,k} = \mathbf{W}^n_{i,1,k}. \tag{3.22}$$

In the vertical z-direction, we follow [22] and use the following balanced Neumann type boundary conditions,

$$\begin{aligned}
\mathbf{B}^n_{i,j,0} = \mathbf{B}^n_{i,j,1}, \mathbf{B}^n_{i,j,N_z+1} = \mathbf{B}^n_{i,j,N_z},\\
\mathbf{u}^n_{i,j,0} = \mathbf{u}^n_{i,j,1}, \mathbf{u}^n_{i,j,N_z+1} = \mathbf{u}^n_{i,j,N_z},\\
\rho^n_{i,j,0} = \rho^n_{i,j,1} e^{\frac{\Delta z}{T_{i,j,1} H}}, \rho^n_{i,j,N_z+1} = \rho^n_{i,j,N_z} e^{-\frac{\Delta z}{T_{i,j,N_z} H}},\\
p^n_{i,j,0} = p^n_{i,j,1} e^{\frac{\Delta z}{T_{i,j,1} H}}, \quad p^n_{i,j,N_z+1} = p^n_{i,j,N_z} e^{-\frac{\Delta z}{T_{i,j,N_z} H}}.
\end{aligned} \tag{3.23}$$

This completes the description of the first order scheme (3.1). Some properties of this scheme are summarized in the theorem below,

Theorem 3.1. *Consider the scheme* (3.1) *approximating the system* (2.5). *This scheme has the following properties,*

(i.) *The scheme* (3.1) *is consistent with* (2.4)*, and it is first order accurate in both space and time (for smooth solutions).*

(ii.) *The scheme* (3.1) *is well-balanced and preserves discrete versions of the steady states* (2.12) *in the following sense: Given data satisfying*

$$\mathbf{u}^n_{i,j,k} = 0, \quad \mathbf{B}^n_{i,j,k} = 0, \quad \rho^n_{i,j,k} = \frac{\rho_0 T_0}{T_k} e^{\frac{-\alpha_k}{H}}, \quad p^n_{i,j} = p_0 e^{\frac{-\alpha_k}{H}}, \tag{3.24}$$

with α_k *defined from the piecewise constant temperature distribution,*

$$T(x, y, z) = T(z) = T_k, \quad z_{k-1/2} < z < z_{k+1/2}, \tag{3.25}$$

by the formula (1.5)*, then the numerical update is computed as,* $\mathbf{W}^{n+1}_{i,j,k}$ *is*

$$\mathbf{W}^{n+1}_{i,j,k} \equiv \mathbf{W}^n_{i,j,k} \quad \forall i, j, k.$$

Proof. The proof of (i.) is straightforward except for the consistency of the gravitational source term $\mathbf{S}^g$. Consistency of the source follows from the definition (3.21) and (3.16) and the following elementary identity,

$$\begin{aligned}
\frac{p^{n,-}_{i,j,k+1/2} - p^{n,+}_{i,j,k-1/2}}{\Delta z} &= p^n_{i,j,k} \left(e^{-\frac{\Delta z}{2HT^n_{i,j,k}}} - e^{\frac{\Delta z}{2HT^n_{i,j,k}}} \right)\\
&= -g\rho^n_{i,j,k} \frac{e^{\frac{\Delta z}{2HT^n_{i,j,k}}} - e^{\frac{-\Delta z}{2HT^n_{i,j,k}}}}{\frac{\Delta z}{HT^n_{i,j,k}}} = -g\rho^n_{i,j,k} + \mathcal{O}(\Delta z^2).
\end{aligned} \tag{3.26}$$

The above identity also shows that the gravity source term is second-order accurate.

The discrete steady conservative variables (3.24) do not vary in either the x or y directions. Therefore, the flux differences $\mathbf{F}_{i+1/2,j,k} - \mathbf{F}_{i-1/2,j,k}$ and $\mathbf{G}_{i,j+1/2,k} - \mathbf{G}_{i,j-1/2,k}$ vanish. As $\mathbf{B}_{i,j,k} \equiv 0$ for all cells, we obtain that the discrete Godunov-Powell source terms $\mathbf{S}^{1,2,3}$ also vanish.

The steady state pressure in (3.24) satisfies,

$$P^n_{i,j,k+1} = P^n_{i,j,k} e^{-\frac{\alpha_{k+1} - \alpha_k}{H}}.$$

The definition of α (1.5) in terms of the piecewise constant temperature distribution (3.16) yields,

$$\alpha_{k+1} - \alpha_k = \frac{\Delta z}{2T_k H} + \frac{\Delta z}{2T_{k+1} H}.$$

Substituting the above identity for the steady state pressure, we obtain,

$$P^n_{i,j,k+1} = P^n_{i,j,k} e^{\frac{-\Delta z}{2T_k H}} e^{\frac{-\Delta z}{2T_{k+1} H}}.$$

This implies that the reconstructed pressures from (3.17) satisfy,

$$p^{n,+}_{i,j,k+1/2} = p^n_{i,j,k+1}(e^{\frac{\Delta z}{2T_{k+1} H}}) = p^n_{i,j,k}(e^{\frac{-\Delta z}{2T_k H}} e^{\frac{-Dz}{2T_{k+1} H}} e^{\frac{\Delta z}{2T_{k+1} H}}) = p^n_{i,j,k} e^{\frac{-\Delta z}{2T_k H}} = p^{n,-}_{i,j,k+1/2} = p^n_{i,j,k+1/2}.$$

Hence we can use (3.19) and (3.20) to obtain,

$$\begin{aligned}\mathbf{H}_{i,j,k+1/2} &= \mathbf{H}\left(\rho^n_{i,j,k}, \mathbf{u}^n_{i,j,k}, \mathbf{B}^n_{i,j,k}, p^{n,-}_{i,j,k+1/2}, \rho^n_{i,j,k+1}, \mathbf{u}^n_{i,j,k+1}, \mathbf{B}^n_{i,j,k+1}, p^{n,+}_{i,j,k+1/2}, \widetilde{\mathbf{B}}_{i,j,k+1/2}\right),\\ &= \mathbf{H}\left(\rho^n_{i,j,k}, \mathbf{0}, \mathbf{0}, p^n_{i,j,k+1/2}, \rho^n_{i,j,k+1}, \mathbf{0}, \mathbf{0}, p^n_{i,j,k+1/2}, \widetilde{\mathbf{B}}_{i,j,k+1/2}\right)\\ &= \left\{0, 0, 0, p^n_{i,j,k+1/2}, 0, 0, 0, 0\right\},\end{aligned}$$

Similarly an explicit evaluation of the gravity source term (3.21) yields,

$$\mathbf{S}^{g,n}_{i,j,k} = \left\{0, 0, \frac{p^n_{i,j,k+1/2} - p^n_{i,j,k-1/2}}{\Delta z}, 0, 0, 0, 0, 0\right\}.$$

Therefore combining the above two expressions, we obtain

$$\frac{\mathbf{H}^n_{i,j,k+1/2} - \mathbf{H}^n_{i,j,k-1/2}}{\Delta z} = \mathbf{S}^{n,g}_{i,j,k} \quad \text{for all } i,j \text{ and } j.$$

Combining the above identity with the fact the flux differences in the horizontal directions and the Godunov-Powell source terms are zero at the discrete steady state, we obtain that

$$\mathbf{W}^{n+1}_{i,j,k} = \mathbf{W}^n_{i,j,k}, \quad \forall i, j, k.$$

□

Note that the well-balanced property includes the boundary points also as the Neumann type boundary condition (3.23) is well-balanced. Furthermore, the proof does not assume any prior information about the parameters of the discrete steady state. Given any initial configuration that satisfies (3.24), the scheme (3.1) preserves it. Any piecewise constant temperature distribution and background magnetic field can be taken to define the scheme. For arbitrary temperature distributions, we have to compute a piecewise constant approximation based on cell averages.

A key difference from [20] is the fact that the temperature is allowed to vary arbitrarily in the vertical direction. In fact, the temperature can be discontinuous and can contain large jumps as the data in figure 1. Furthermore, local hydrostatic reconstructions of the density are not necessary on account of the condition (3.20), that the HLL three wave solver satisfies. This concludes the description of the first-order scheme (3.1).

3.2. **The second order scheme.** A first-order accurate scheme like (3.1) may not suffice for realistic computations. We need to extend (3.1) to second-order of accuracy. At any time t, given the cell averages $\mathbf{W}_{i,j,k}(t)$, the semi-discrete form of the second order scheme is given by

$$\begin{aligned}\frac{d}{dt}\mathbf{W}_{i,j,k} = \boldsymbol{\mathcal{F}}_{i,j,k} = &-\frac{1}{\Delta x}(\widetilde{\mathbf{F}}_{i+1/2,j,k} - \widetilde{\mathbf{F}}_{i-1/2,j,k}) - \frac{1}{\Delta y}(\widetilde{\mathbf{G}}_{i,j+1/2,k} - \widetilde{\mathbf{G}}_{i,j-1/2,k})\\ &- \frac{1}{\Delta z}(\widetilde{\mathbf{H}}_{i,j,k+1/2} - \widetilde{\mathbf{H}}_{i,j,k-1/2}) + \widetilde{\mathbf{S}}^1_{i,j,k} + \widetilde{\mathbf{S}}^2_{i,j,k} + \widetilde{\mathbf{S}}^3_{i,j,k} + \mathbf{S}^g_{i,j,k}.\end{aligned} \tag{3.27}$$

The numerical fluxes $\mathbf{F}, \mathbf{G}, \mathbf{H}$ and the sources $\widetilde{\mathbf{S}}^{1,2,3}$ are defined below. The time dependence in the above expression is suppressed for notational convenience.

It is standard (see [32]) to replace the piecewise constant approximation $\mathbf{W}_{i,j,k}$ with a non-oscillatory piecewise linear reconstruction in-order to obtain second-order spatial accuracy. There are a variety of reconstructions including the popular TVD-MUSCL limiters [58], ENO reconstruction [26] and WENO reconstruction [50]. However, we need (3.27) to preserve a suitable discrete version of (2.12) and a standard reconstruction of the conservative variables does not lead to a well-balanced scheme.

Consequently we will modify the novel *equilibrium variables* based reconstruction algorithm of [22] to the setting of non-isothermal atmospheres below. Given the cell averages $\mathbf{W}_{i,j,k}$ at any given time, we define a piecewise constant local temperature distribution by (3.16) and denote the cell temperature as $T_{i,j,k}$. We have the following reconstruction algorithms.

3.3. **Minmod reconstruction (MM).** Given the cell values $q_{i,j,k}$ of a state variable q, denote the *minmod* derivatives as

(3.28)
$$D^x q_{i,j,k} = \text{minmod}\left(\frac{q_{i+1,j,k}-q_{i,j,k}}{\Delta x}, \frac{q_{i,j,k}-q_{i-1,j,k}}{\Delta x}\right), \quad D^y q_{i,j,k} = \text{minmod}\left(\frac{q_{i,j+1,k}-q_{i,j,k}}{\Delta y}, \frac{q_{i,j,k}-q_{i,j-1,k}}{\Delta y}\right),$$
$$D^z q_{i,j,k} = \text{minmod}\left(\frac{q_{i,j,k+1}-q_{i,j,k}}{\Delta z}, \frac{q_{i,j,k}-q_{i,j,k-1}}{\Delta z}\right), \quad \text{minmod}(a,b) = \frac{1}{2}(\text{sgn}(a)+\text{sgn}(b))\min(|a|,|b|).$$

Then a piecewise linear *non-oscillatory* approximation of q is of the form,

$$q(x,y,z) = q_{i,j,k}(x,y,z) = q_{i,j,k} + D^x q(x-x_i) + D^y q(y-y_j) + D^z q(z-z_k), \quad (x,y,z) \in \mathcal{C}_{i,j,k}. \tag{3.29}$$

From the cell values of $\rho, \mathbf{u}$ and $\mathbf{B}$, we define the minmod slopes by (3.28) and obtain the corresponding piecewise linear approximations of these variables by (3.29). However, a minmod reconstruction of the pressure does not lead to a well balanced scheme. We need a novel pressure reconstruction, based on a corresponding reconstruction of the temperature.

Given the cell averages $\mathbf{W}_{i,j,k}$, compute the cell temperature $T_{i,j,k}$ by (3.16). We define a continuous piecewise linear reconstruction of the temperature $\hat{T}_{i,j}(z)$, taking the values $\hat{T}_{i,j,k}$ at the cell centers. This piecewise linear temperature can be used to compute the corresponding α function by (1.5). However, we only need the differences in α given by,

$$\alpha_{i,j,k+\lambda} - \alpha_{i,j,k} = \int_{z_k}^{z_{k+\lambda}} \frac{1}{\hat{T}_{i,j}(z)} dz = \frac{\Delta z}{T_{i,j,k+1}-T_{i,j,k}} \log\left(\frac{\hat{T}_{i,j}(z_{k+\lambda})}{T_{i,j,k}}\right), \quad \lambda \in \{1/2, 1\}. \tag{3.30}$$

Note that the difference in α is always well-defined and for $T_{i,j,k+1} = T_{i,j,k}$ degenerates to

$$\alpha_{i,j,k+\lambda} - \alpha_{i,j,k} = (z_{i,j,k+\lambda} - z_{i,j,k})/T_{i,j,k}, \quad \lambda \in \{1/2, 1\}. \tag{3.31}$$

We use the α function to reconstruct the pressure.

As in [22], we define

$$\mathbf{L}p_{i,j,k} = \log(p_{i,j,k}), \tag{3.32}$$

and compute the minmod derivatives $D^{x,y}\mathbf{L}p$ by (3.28). A scaled minmod derivative in the z-direction takes the form,

$$D^z \mathbf{L}p_{i,j,k} = \text{minmod}\left(\frac{\mathbf{L}p_{i,j,k+1}-\mathbf{L}p_{i,j,k}}{\alpha_{i,j,k+1}-\alpha_{i,j,k}}, \frac{\mathbf{L}p_{i,j,k}-\mathbf{L}p_{i,j,k-1}}{\alpha_{i,j,k}-\alpha_{i,j,k-1}}\right), \tag{3.33}$$

where the difference in α is computed in (3.30). Then a piecewise linear approximation of the pressure is computed by

$$p(x,y,z) = p_{i,j,k} e^{D^x \mathbf{L}p_{i,j,k}(x-x_i)} e^{D^y \mathbf{L}p_{i,j,k}(y-y_j)} e^{D^z \mathbf{L}p_{i,j,k}(\alpha(z)-\alpha(z_k))}, \tag{3.34}$$

where α is again computed from (3.30). The cell edge values of the conservative variables can be easily obtained from the piecewise linear approximations of the primitive variables. The minmod limiter is one possible choice among many reconstruction procedures. Other limiters like the MC, superbee, ENO and WENO limiters can be modified analogously.

We denote the reconstructed piecewise linear conservative variables in the cell $\mathcal{C}_{i,j,k}$ as $\mathbf{W}_{i,j,k}(x,y,z)$ and define the following corner values,

$$\mathbf{W}^E_{i,j,k} = \mathbf{W}_{i,j,k}(x_{i+1/2}, y_j, z_k), \quad \mathbf{W}^W_{i,j,k} = \mathbf{W}_{i,j,k}(x_{i-1/2}, y_j, z_k),$$
$$\mathbf{W}^N_{i,j,k} = \mathbf{W}_{i,j,k}(x_i, y_{j+1/2}, z_k), \quad \mathbf{W}^S_{i,j,k} = \mathbf{W}_{i,j,k}(x_i, y_{j-1/2}, z_k),$$
$$\mathbf{W}^t_{i,j,k} = \mathbf{W}_{i,j,k}(x_i, y_j, z_{k+1/2}), \quad \mathbf{W}^b_{i,j,k} = \mathbf{W}_{i,j,k}(x_i, y_j, z_{k-1/2}),$$

and define the numerical fluxes by

$$\begin{aligned}\widetilde{\mathbf{F}}_{i+1/2,j,k} &= \mathbf{F}\left(\mathbf{W}^E_{i,j,k}, \mathbf{W}^W_{i+1,j,k}, \widetilde{\mathbf{B}}_{i+1/2,j,k}\right), \qquad \widetilde{\mathbf{G}}_{i,j+1/2,k} = \mathbf{G}\left(\mathbf{W}^N_{i,j,k}, \mathbf{W}^S_{i,j+1,k}, \widetilde{\mathbf{B}}_{i,j+1/2,k}\right),\\ \widetilde{\mathbf{H}}_{i,j,k+1/2} &= \mathbf{H}\left(\mathbf{W}^t_{i,j,k}, \mathbf{W}^b_{i,j,k+1}, \widetilde{\mathbf{B}}_{i,j,k+1/2}\right),\end{aligned} \tag{3.35}$$

where $\mathbf{F}, \mathbf{G}$,and $\mathbf{H}$ are given by the three wave solver of the previous section. The value of the staggered coefficient $\widetilde{\mathbf{B}}$ is given by a simple evaluation,

$$\widetilde{\mathbf{B}}_{i+1/2,j,k} = \widetilde{\mathbf{B}}(x_{i+1/2}, y_j, z_k), \quad \widetilde{\mathbf{B}}_{i,j+1/2,k} = \widetilde{\mathbf{B}}(x_i, y_{j+1/2}, z_k), \quad \widetilde{\mathbf{B}}_{i,j,k+1/2} = \widetilde{\mathbf{B}}(x_i, y_j, z_{k+1/2}),$$

This choice ensures formal second order accuracy for a smooth background magnetic field.

The discrete Godunov-Powell source terms in (3.27) can be defined in analogy with the first-order case by replacing the cell averages with the corresponding corner point values defined above. A correction (see [21, 22]) is needed to ensure consistency. The discretized gravity source term $\mathbf{S}^g$ is given by,

$$\mathbf{S}^g_{i,j,k} = \left\{0, 0, \frac{p^t_{i,j,k} - p^b_{i,j,k}}{\Delta z}, 0, 0, 0, 0, -\rho^n_{i,j,k}(u^n_3)_{i,j,k} g\right\}. \tag{3.36}$$

This source can be shown to be consistent with the gravity source term in (2.5) to second order by modifying (3.26).

Summarizing, we perform a standard piecewise linear reconstruction, except for the hydrostatic reconstruction of the pressure, given by (3.30)-(3.34).

3.3.1. *Boundary conditions for the second order scheme.* The boundary is treated in the following way. We need to specify two layers of ghost cells in each direction for a second order scheme. We use periodic boundary conditions in the x- and y- directions, i.e., for $1 \le j \le N_y$ and $1 \le k \le N_z$, we have

$$\mathbf{W}_{0,j,k} = \mathbf{W}_{N_x,j,k}, \quad \mathbf{W}_{-1,j,k} = \mathbf{W}_{N_x-1,j,k}, \quad \mathbf{W}_{N_x+1,j,k} = \mathbf{W}_{1,j,k}, \quad \mathbf{W}_{N_x+2,j,k} = \mathbf{W}_{2,j,k} \tag{3.37}$$

The ghost cell values in the y-direction can be defined analogously.

In the z-direction, we use second-order extrapolated Neumann boundary conditions for the velocity and the magnetic field, i.e., for $\mathbf{w} = \{\mathbf{u}, \mathbf{B}\}$,

$$\mathbf{w}_{i,j,d} = \mathbf{w}_{i,j,1}, \quad \mathbf{w}_{i,j,N_z+2+d} = \mathbf{w}_{i,j,N_z} \tag{3.38}$$

for $1 \le i \le N_x,\ 1 \le j \le N_y$ and $d \in \{0, -1\}$ in order to define the values in the ghost cells.

The pressure and the density in the ghost cells are extrapolated in terms of its logarithm $\mathbf{L}p = \log(p)$ and $\mathbf{L}\rho = \log(\rho)$ according to (3.34) and simplify to

$$\begin{aligned}p_{i,j,d} &= p_{i,j,1} e^{(\alpha_{i,j,d} - \alpha_{i,j,1})/H}, \quad p_{i,j,N_z+2+d} = p_{i,j,N_z} e^{(\alpha_{i,j,N_z+2+d} - \alpha_{i,j,N_z})/H},\\ \rho_{i,j,d} &= \rho_{i,j,1} e^{(\alpha_{i,j,d} - \alpha_{i,j,1})/H}, \quad \rho_{i,j,N_z+2+d} = \rho_{i,j,N_z} e^{(\alpha_{i,j,N_z+2+d} - \alpha_{i,j,N_z})/H},\end{aligned} \tag{3.39}$$

where the differences in α are given by (3.31). This amounts to using a scaled version of the extrapolated Neumann type boundary conditions of [20] for the primitive variables.

3.3.2. *Time Stepping.* The standard scheme for a first order approximation in time is the forward Euler time stepping, formally written as

$$\mathbf{W}^{n+1}_{i,j,k} = \mathbf{W}^n_{i,j,k} + \Delta t^n \boldsymbol{\mathcal{F}}^n_{i,j,k}$$

where $\boldsymbol{\mathcal{F}}^n_{i,j,k}$ is defined in (3.27). For second-order schemes, we use the second-order strong-stability preserving Runge-Kutta (SSP) time stepping (see [25])

$$\begin{aligned}\mathbf{W}^*_{i,j,k} &= \mathbf{W}^n_{i,j,k} + \Delta t^n \boldsymbol{\mathcal{F}}^n_{i,j,k},\\ \mathbf{W}^{**}_{i,j,k} &= \mathbf{W}^*_{i,j,k} + \Delta t^n \boldsymbol{\mathcal{F}}^*_{i,j,k},\\ \mathbf{W}^{n+1}_{i,j,k} &= \frac{1}{2}(\mathbf{W}^n_{i,j,k} + \mathbf{W}^{**}_{i,j,k}).\end{aligned}$$

The time step is determined by a standard CFL condition.

The properties of the second-order scheme are summarized in the theorem below,

Theorem 3.2. *Consider the scheme* (3.27) *approximating the system* (2.5). *This scheme has the following properties,*

(i.) *The scheme* (3.27) *is consistent with* (2.5) *and is second-order accurate.*
(ii.) *The scheme* (3.27) *is well-balanced and preserves a second order accurate version of the steady state* (2.12)*, i.e, given data satisfying*

$$\mathbf{u}_{i,j,k} = 0, \quad \mathbf{B}_{i,j,k} = 0, \quad \rho_{i,j,k} = \rho_0 e^{\frac{-\alpha_k}{H}}, \quad p_{i,j,k} = p_0 e^{\frac{-\alpha_k}{H}}, \quad \text{for all } i,j \text{ and } k, \tag{3.40}$$

with α_k *defined by* (3.30)*, and any background field* $\widetilde{\mathbf{B}}$*, then the approximate solutions computed by* (3.27) *satisfy,*

$$\frac{d}{dt}\mathbf{W}_{i,j,k} \equiv 0, \tag{3.41}$$

for all i, j *and* k.

Proof. The proof of the second-order accuracy is straightforward. As the data satisfy (3.40), we obtain

$$\mathbf{L}p_{i,j,k} = \mathbf{L}p_k = \log(p_k) = \log(p_0) - \frac{\alpha_k}{H}.$$

Therefore, the minmod slopes (3.33) lead to

$$D^z \mathbf{L}p_k = \text{minmod}\left(-\frac{1}{H}, -\frac{1}{H}\right) = -\frac{1}{H}. \tag{3.42}$$

Hence, the reconstructed pressure (3.34) is of the form,

$$p_{i,j,k}(x,y,z) = p_k(z) = p_k e^{-\frac{\alpha(z)-\alpha_k}{H}}. \tag{3.43}$$

Therefore, using (3.40), we obtain

$$p^b_{i,j,k+1} = p^b_{k+1} = p_{k+1} e^{\frac{\alpha_{k+1}-\alpha_{k+1/2}}{H}} = p_k e^{-\frac{\alpha_{k+1}-\alpha_k}{H}} e^{\frac{\alpha_{k+1}-\alpha_{k+1/2}}{H}} = p_k e^{-\frac{\alpha_{k+1/2}-\alpha_k}{H}} = p^t_k = p_{k+1/2}.$$

As $\mathbf{u}_{i,j,k} = \mathbf{B}_{i,j,k} \equiv 0$, the reconstructed velocity and magnetic fields are identically zero. We combine the above facts with (3.19) and (3.20) to obtain,

$$\mathbf{H}_{i,j,k+1/2} = \{0, 0, 0, p_{k+1/2}, 0, 0, 0, 0\}.$$

Therefore, (3.36) yields,

$$\frac{\mathbf{H}_{i,j,k+1/2} - \mathbf{H}_{i,j,k-1/2}}{\Delta z} = \mathbf{S}^g_{i,j,k}, \quad \forall i,j,k.$$

The data do not vary in the x and y directions. Hence, the flux differences in these directions vanish. Similarly, the Godunov-Powell source terms in each direction are identically zero as $\mathbf{B} \equiv 0$. Substituting all the above identities in (3.27) leads to (3.41).

□

3.4. **Implementation.** The well-balanced high-order schemes presented above are implemented in a modular C++ based code termed *SURYA*,[52]. The code includes a set of approximate Riemann solvers, high-order non-oscillatory reconstruction and time integration routines. Realistic initial and boundary conditions are also specified. A wide range of background magnetic fields $\widetilde{B}$ are included. The code is parallelized with the MPI library, using a domain decomposition technique. The parallelization is also straightforward as the schemes are explicit and do not need any staggered grids. A python front end to the code is included for configuring data and results are visualized using matplotlib for two-dimensional visualizations and MAYAVI for three-dimensional visualizations. All the results presented below are from experiments performed on the TITAN cluster of the University of Oslo.

4. Two dimensional numerical results

We test the first order (3.1) and second order (3.27) schemes on a suite of numerical experiments. For the sake of comparison, we consider a standard *unbalanced* version of the first order scheme similar to (3.1) based on the HLL three wave solver and upwind discretizations of the Godunov-Powell source terms. This scheme does not use local hydrostatic reconstructions of the pressure (3.17) and discretizes gravity by the simpler form,

$$\widetilde{\mathbf{S}}^{g}_{i,j} = \{0, 0, 0, -\rho_{i,j,k} g, 0, 0, 0, -\rho_{i,j,k} (u_3)_{i,j,k}\ g\}\,. \tag{4.1}$$

Similarly, we consider a second-order version of the above *unbalanced* scheme based on the minmod reconstruction in the conservative variables, as opposed to the novel pressure reconstruction of the scheme (3.27). Hence, we test the following four schemes:

H_3	First order *unbalanced* HLL three wave solver,
$H_{3\mathrm{WB}}$	well-balanced version of H_3 (3.1),
H_3M	second order *unbalanced* HLL three-wave solver with Minmod reconstruction.
$H_{3\mathrm{WB}}M$	second order well-balanced HLL three-wave solver (3.27) with Minmod reconstruction.

The first order schemes are evolved with a CFL number of 0.45 and the second order schemes use a CFL number of 0.9. In all our computations we set $\gamma = 5/3$.

As stated earlier, the main difference between this paper and [22] lies in the study of non-isothermal atmospheres. We choose a *realistic* steady state temperature distribution $T(z)$ that is modeled on the observed temperature presented in figure 1. Our model steady state temperature, shown in figure 2, is given by

$$T(z) = \begin{cases} 1, & \text{if } z \le 1 \\ +99 \cdot 8 \cdot (z-1)^2 + 1, & \text{if } 1 < z \le 1.25 \\ -99 \cdot 8 \cdot (z-1.5)^2 + 100, & \text{if } 1.25 < z \le 1.5 \\ 100, & \text{if } 1.5 < z \end{cases}$$

The model temperature distribution approximates the observed temperature qualitatively and consists of two regions of constant temperature (modeling the chromosphere and the corona, respectively), separated by a rapidly varying gradient (modeling the transition region). Furthermore, the non-dimensional temperature jump is of two orders of magnitude, replicating the corresponding jump in figure 1. The corresponding steady state pressure and density are readily calculated from (2.12).

All the quantities are non-dimensionalized suitably from the realistic solar parameters used in [7]. The constants are acceleration due to gravity, $g = 2.74$, constant $H = 0.158$ and initial pressure $p_0 = 1.13$. All subsequent two-dimensional experiments are performed on the domain $[x, z] \in [0, 4] \times [0, 8]$. At the steady state, we assume that there is no variation in the y-direction.

Regarding the measurement of errors, if we have a reference solution available, then we define the relative error as

$$100 \times \frac{\|\alpha - \alpha_{\mathrm{ref}}\|}{\|\alpha_{\mathrm{ref}}\|},$$

where α is (a component of) the numerical approximation and α_{ref} is (the same component of) the reference solution, and $\|\cdot\|$ is some (usually L^1) norm.

4.1. Hydrodynamics: steady state.

We begin with a zero background magnetic field $\widetilde{B}$ and test the well-balancing properties of the schemes. The initial conditions are given by (2.12) and the parameters are chosen as above. The steady state temperature is given in figure 2. We show the relatives errors in the L^1 norm for the pressure in table 1. The reference solution is the steady state pressure distribution (2.12), with α evaluated in an appropriate discrete form. The table clearly shows that both the *well-balanced* $H_{3\mathrm{WB}}$ and $H_{3\mathrm{WB}}M$ schemes maintain the steady state to machine precision. The *unbalanced* H_3 and H_3M schemes generate large errors and do not preserve a discrete steady state. Although the errors seem to decrease with decreasing mesh size, they are still quite large on very fine meshes. This makes the *unbalanced* schemes unsuitable for wave propagation experiments as waves are realized as small perturbations of the steady state (see [20]).

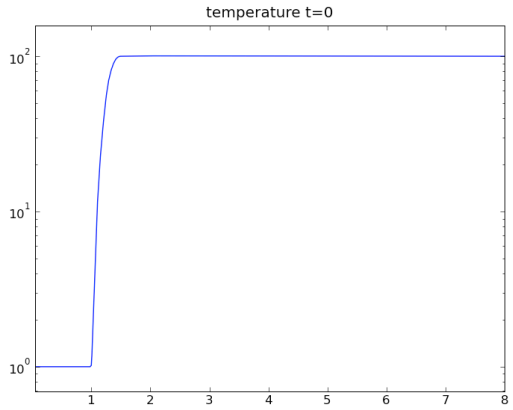

FIGURE 2. Steady state temperature distribution for the model atmosphere.

% L^1-error in p	H_3	H_3M	$H_{3\mathrm{WB}}$	$H_{3\mathrm{WB}}M$
100x200	4.9e+2	8.2e+0	7.0e-13	1.1e-12
200x400	1.6e+2	1.1e+0	3.7e-14	7.2e-14
400x800	6.7e+1	1.4e-1	4.8e-13	4.3e-13
800x1600	3.0e+1	1.7e-2	6.4e-13	7.1e-13

TABLE 1. Relative L^1 errors in pressure at the hydrodynamic steady state for a sequence of meshes.

4.2. **Hydrodynamics: wave propagation.** Next, we simulate waves in the model non-isothermal hydro-atmosphere. The background magnetic field $\widetilde{\mathbf{B}}$ is set to zero and the waves are modeled ([7, 20, 22]) by perturbing the bottom vertical boundary. The bottom boundary acts a piston and sends temporally sinusoidal waves up the domain. This perturbation is expressed by the following boundary condition for the normal velocity field,

$$u^{3,n}_{i,j,\{0,-1\}} = 0.3e^{-100(x_{i,j,\{0,-1\}}-1.9)^2}\sin\left(6\pi t^n\right)\mathbf{1}_{\{[1.65,2.15]\}}. \tag{4.2}$$

Note that the wave source is spatially localized as in [7]. The waves move up and are influenced by the background state. The results for the normal velocity u_3 for a 400×800 mesh at time $t = 1.17$ are shown in figure 3. The figure clearly shows that the waves are resolved quite well by the well-balanced schemes. The first-order $H_{3\mathrm{WB}}$ is diffusive whereas the second-order $H_{3\mathrm{WB}}M$ resolves the wave fronts very sharply. At the time depicted in the plot, the piston has sent in a train of waves that have traveled up the atmosphere. The waves spread out with spherical wave fronts till they reach the *model transition region* (depicted in gray) where they encounter the rapid jump in temperature and speed up considerably. The wave acceleration is depicted very well in figure 3. This acceleration is to be expected as the wave velocity scales as a square root of the local temperature. A jump of two orders of magnitude in the temperature leads to an increase in speed by an order of magnitude. The results in figure 3 illustrate that the well-balanced schemes are quite robust with respect to this jump in the temperature. The second-order scheme resolves the accelerating wave fronts quite sharply whereas the first-order scheme is more diffusive in the model corona than in the model chromosphere.

4.3. **Magneto-hydrodynamics: steady state.** The above experiment illustrated the non-trivial role played by temperature variations in the acceleration of waves as they hit the transition region. Next, we study the impact of magnetic fields on wave propagation. We start with an approximation to the steady state (1.8) realized by specifying a non-zero background magnetic field $\widetilde{\mathbf{B}}$ in (2.4). Following [7, 20, 22], we choose a

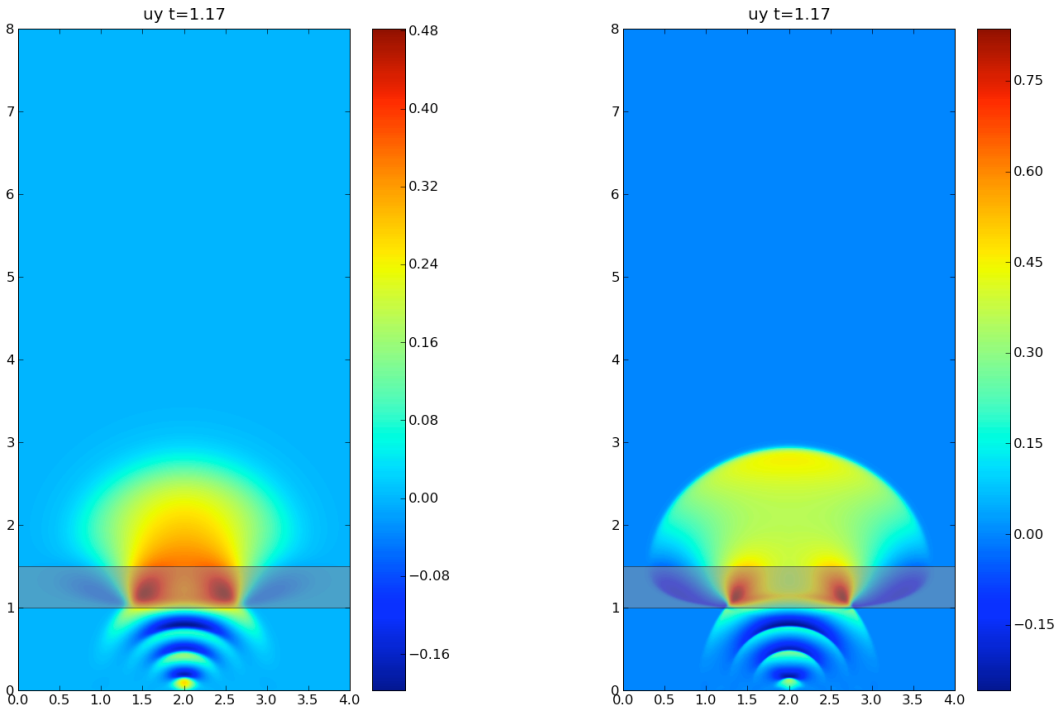

(a) $H_{3\mathrm{WB}}$ (b) $H_{3\mathrm{WB}}M$

FIGURE 3. Hydrodynamic wave propagation. Normal velocity field u_3 on a 400×800 mesh at time $t = 1.17$.

realistic two-dimensional background magnetic field of the form (2.11) as follows: We let $\widetilde{B}_3(x, y)$ approximate

$$\bar{B}_3(x, y, 0) = \begin{cases} 2.7e^{-(x-4)^2} - 1.9e^{-((x-2.7)/0.37)^2} - 1.9e^{-((x-5.3)/0.37)^2} - 0.0168565, & \text{if } 1.84 \leq x < 6.17 \\ 0, & \text{otherwise.} \end{cases} \tag{4.3}$$

up to the first fourteen terms in the Fourier series. The Fourier coefficients of $\widetilde{B}_1$ and $\widetilde{B}_2$ follow from the potential field assumption as in (2.11). The resulting potential field consists of a large unipolar magnetic flux concentration surrounded on each side by two smaller concentrations of opposite polarity field (see [7], figure 1 for an illustration). The initial conditions are set to the steady state (2.12) and the errors in the pressure are shown in table 2. The table shows that the unbalanced schemes lead to large errors whereas the well-balanced schemes preserve the magneto-hydrodynamic steady state to machine precision, even for a complex magnetic field and a complex temperature distribution.

4.4. **Wave propagation with magnetic fields.** Following, [7] and [22], we consider two different configurations for the magnetic field. First, we take a *weak* magnetic field, termed $\mathbf{FR}_2$, derived as in the previous section from (4.3). This field is termed weak relative to a *strong* field, which we take as $\mathbf{FR}_2$ multiplied by 3. Hence, the two fields have the same topology. The waves are induced as perturbations of the bottom boundary,

$$\mathbf{u}^n_{i,j,\{0,-1\}} = 0.3 \frac{\mathbf{B}^n_{i,j,k,\{0,-1\}}}{|\mathbf{B}^n_{i,j,k,\{0,-1\}}|} \sin(6\pi t^n)\, \mathbf{1}_{\{[1.65,2.15]\}}. \tag{4.4}$$

% L^1-error in p	H_3	H_3M	$H_{3\mathrm{WB}}$	$H_{3\mathrm{WB}}M$
100x200	3.5e+2	6.3e+0	9.8e-20	2.5e-18
200x400	1.2e+2	8.1e-1	1.6e-18	3.6e-18
400x800	4.9e+1	1.2e-1	3.5e-18	3.5e-18
800x1600	2.2e+1	1.5e-2	1.4e-17	4.6e-18

TABLE 2. Relative L^1 errors in pressure at the magneto-hydrodynamic steady state for a sequence of meshes

Observe that the factor "$B/|B|$" makes sure that the waves are sent in aligned with the magnetic field. The results with the well-balanced $H_{3\mathrm{WB}}$ and $H_{3\mathrm{WB}}M$ schemes for the weak and strong magnetic fields are presented in figures 4 and 5 respectively.

The figures 4 and 5 show the velocity $\mathbf{u}$ in the direction of the magnetic field $\mathbf{B}$ and the velocity perpendicular to the magnetic field, denoted as $\mathbf{u}^{\parallel}$ and $\mathbf{u}^{\perp}$ respectively. The temperature is also shown. The results at time $t = 1.71$, computed with the well-balanced $H_{3\mathrm{WB}}$ and $H_{3\mathrm{WB}}M$ schemes on a 400×800 mesh are presented. The numerical resolution for both magnetic configurations is quite good. The first-order results are dissipative, but show qualitative agreement. The second-order $H_{3\mathrm{WB}}M$ is much more accurate and the waves and fronts are resolved very sharply. The non-reflecting boundary conditions at the top boundary work quite well. They are stable and the magnitude of reflections is low. Several waves exit the top boundary without large reflections allowing us to perform much longer time simulations than performed previously. However, there are still some reflections (bottom right of figure 5) and we are currently addressing the issue of minimizing reflections.

In both cases, the waves behave differently in the model chromosphere than in the corona. In particular, the wave speeds are much (an order of magnitude) higher in the corona than in the chromosphere. At low β, the velocity in the direction of the magnetic field depicts the slow modes of the system. From figure 4 (left column), we observe that the magnetic field is not strong enough to focus the waves in this case. Furthermore the waves interact with the *magnetic canopy* (the $\beta = 1$ isoline) in this case. As observed in [7, 22], there is a large amount of mode mixing between the fast and slow mode. On reaching the *model transition region* (again marked in grey), the waves of both families are accelerated. The transition region does not seem to contribute to any further mode mixing. The velocity, perpendicular to the direction of the magnetic field (shown in the middle column of both figures) illustrates the formation of fast waves. As the slow waves hit the magnetic canopy, mode conversion takes place and fast waves are formed. This differential in the velocities at the magnetic canopy leads to *wave turning*. This turning effect was observed in [7] and is also seen here. The perpendicular component is very small in the top region of the atmosphere. The right column of figure 4 shows the variation of the temperature in the domain. The temperature varies on account of wave motion. The variation in the temperature is about five percent of the initial temperature. Furthermore, the transition region is no longer static but is perturbed by the incoming wave. The main difference between the strong and weak magnetic field cases lies in the focusing of the waves. As shown in figure 5 (left column), the waves in the chromosphere are focused by the strong magnetic field. The waves hit the transition region and are accelerated. The magnetic field is such that there is much less interaction between the waves and the $\beta = 1$ isolines. Hence, mode mixing is less pronounced in this case. The temperature variation is clearly visible in figure 5 (right column). The perturbations of the transition regions are also larger, when compared to the weak magnetic field. This demonstrates that the magnetic field plays a prominent role in the temperature variation in the atmosphere.

The key difference between the results of [7],[22] and those presented here lie in the introduction of temperature variation in the atmosphere. The waves interact with the temperature jump and are accelerated. The magnetic field influences this interaction considerably. This phenomena is best depicted by the *movement* of the transition region. The results in figure 4 and 5 clearly demonstrate that the transition region is far from static and *moves* during the computation. The motion seems to be sinusoidal as the incoming waves vary sinusoidally in time. The motion of the transition region is due to the movement of matter by waves. This is shown in figure 6, where we plot the relative change in density with respect to the steady state density (2.12), for both strong and weak magnetic field configurations. Both results are with the $H_{3\mathrm{WB}}M$ scheme and show that the movement of matter and the transition layer in the bottom right of figures 4 and 5 are correlated.

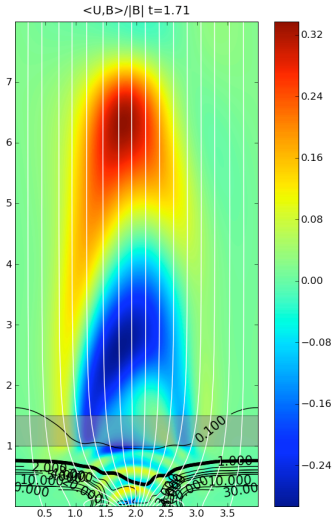

(a) $\mathbf{u}^{\parallel}, H_{3\mathrm{WB}}$

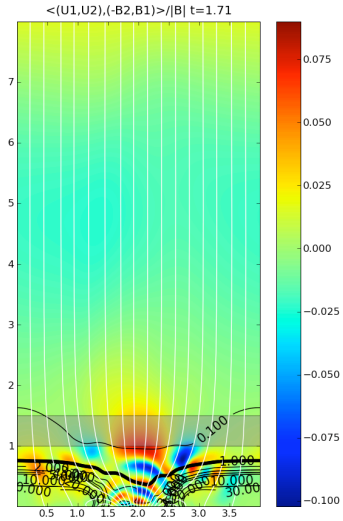

(b) $\mathbf{u}^{\perp}, H_{3\mathrm{WB}}$

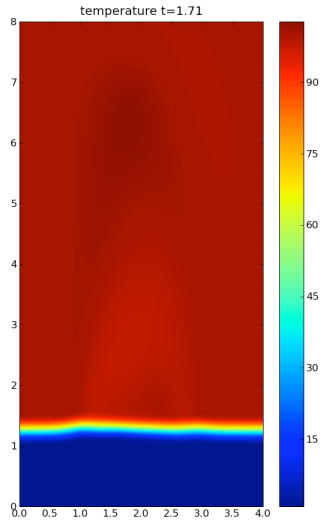

(c) $T, H_{3\mathrm{WB}}$

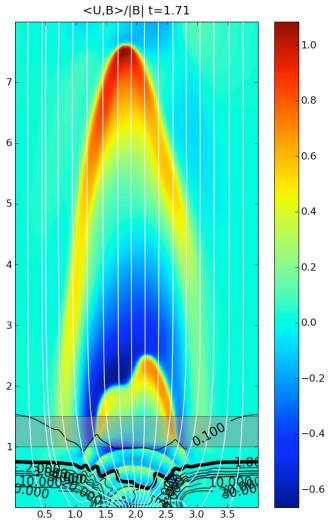

(d) $\mathbf{u}^{\parallel}, H_{3\mathrm{WB}}M$

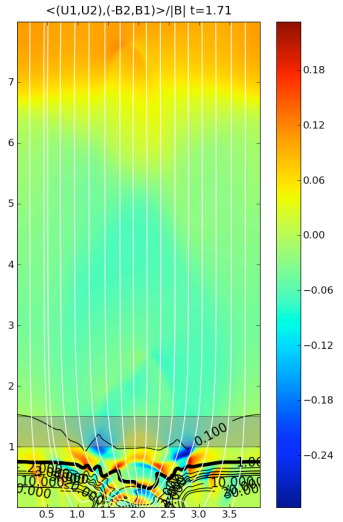

(e) $\mathbf{u}^{\perp}, H_{3\mathrm{WB}}M$

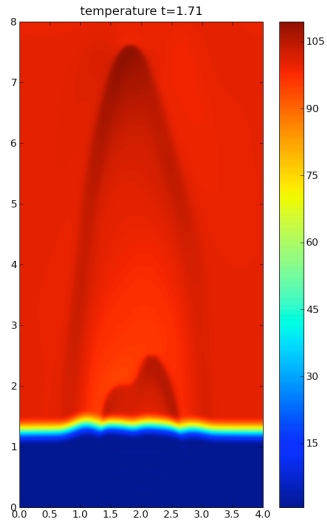

(f) $T, H_{3\mathrm{WB}}M$

FIGURE 4. wave propagation with weak magnetic field on a 400×800 mesh at time $t = 1.71$.

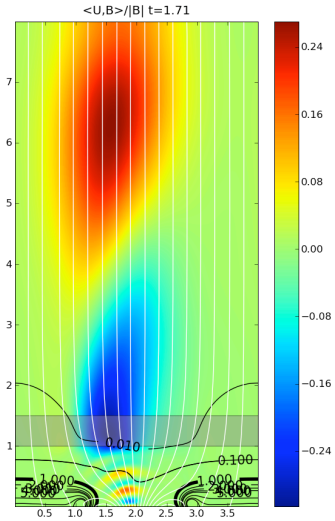

(a) $\mathbf{u}^{\parallel}, H_{3\mathrm{WB}}$

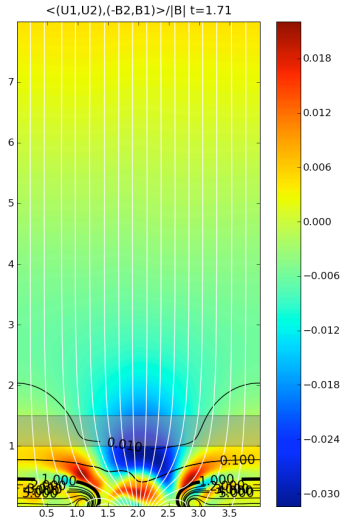

(b) $\mathbf{u}^{\perp}, H_{3\mathrm{WB}}$

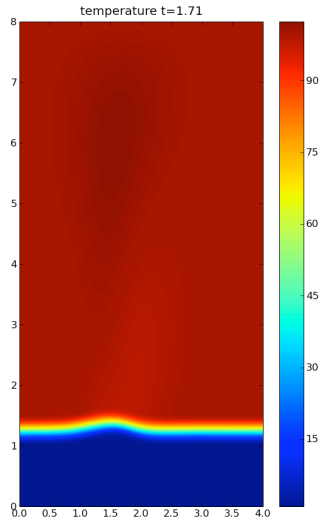

(c) $T, H_{3\mathrm{WB}}$

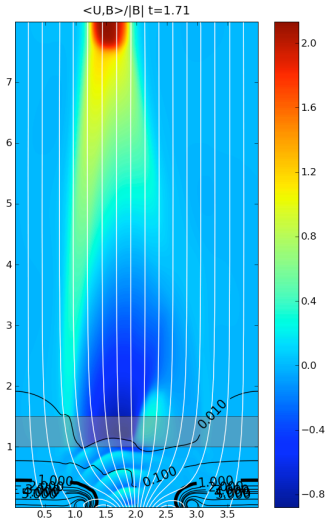

(d) $\mathbf{u}^{\parallel}, H_{3\mathrm{WB}}M$

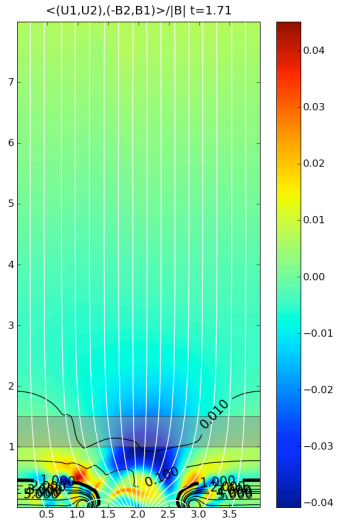

(e) $\mathbf{u}^{\perp}, H_{3\mathrm{WB}}M$

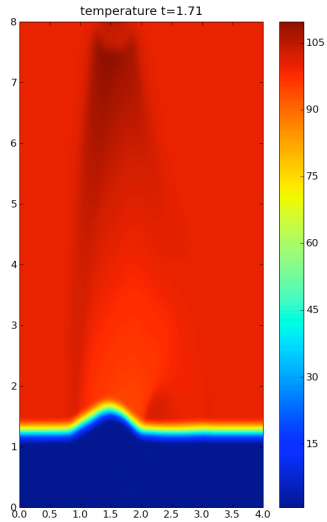

(f) $T, H_{3\mathrm{WB}}M$

FIGURE 5. wave propagation with strong magnetic field on a 400×800 mesh at time $t = 1.71$.

Furthermore, this movement is much more focused for the strong magnetic field. The weak magnetic field is unable to constrain matter in a preferred direction and the corresponding waves move matter along the cross section whereas the strong magnetic field ensures that matter moves only in a certain part of the cross section due to the focusing of the waves. Consequently, the amplitude of the variation of the transition layer is greater.

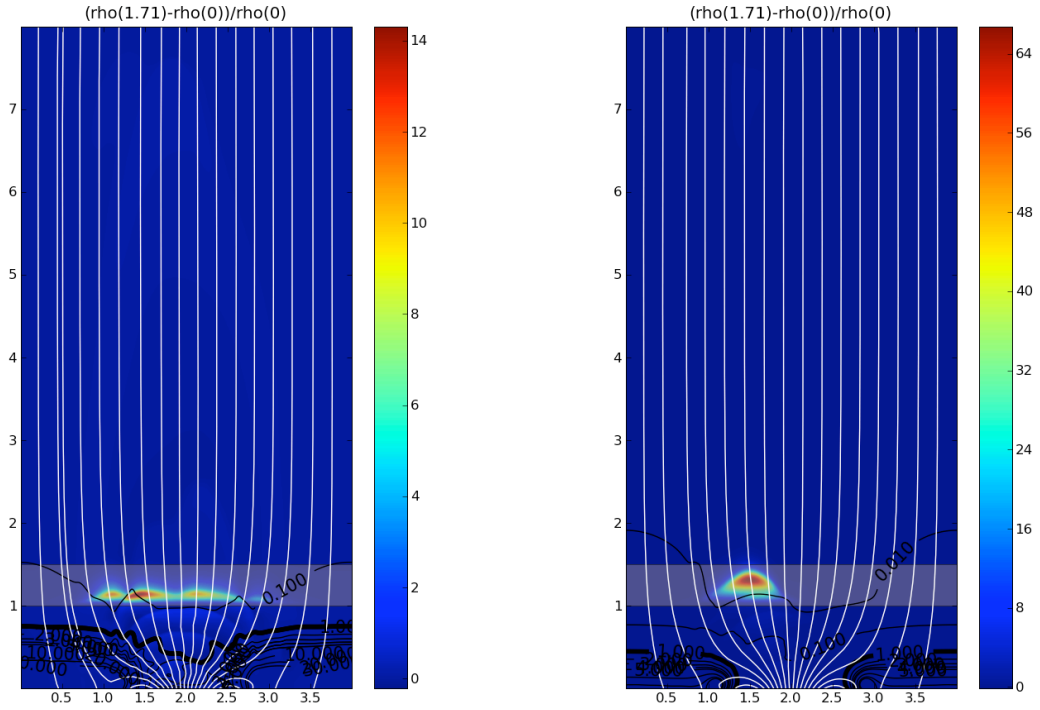

(a) weak field

(b) strong field

FIGURE 6. Relative change in density at time $t = 1.71$ computed with $H_{3\mathrm{WB}}M$ on a 400×800 mesh.

5. Three dimensional numerical results

We present numerical experiments for a three-dimensional non-isothermal magneto-atmosphere in this section. The background magnetic field $\widetilde{B}$ in (2.4) is expressed by (2.11). The co-efficients in (2.11) are computed as the modes of the function

$$B_3(x, y, 0) = e^{-r^2} - 0.25e^{-8(r-1.5)^2}, \text{ where } r = \sqrt{(x-4)^2 + (y-4)^2}. \tag{5.1}$$

The computational domain is $(x, y, z) \in [0, 4] \times [0, 4] \times [0, 8]$ and the parameters g, H and p_0 are similar to the previous section. Furthermore, the steady temperature distribution is identical to the one used in the previous section and shown in figure 2. We test for the two configurations: the weak background field, $\mathbf{FR}_3$, with co-efficients given by the first 16×16 coefficients of (5.1) and the strong background field with co-efficients $\mathbf{3FR}_3$, in analogy with the previous section. The magnetic field configurations, together with $\beta = 1$, at the steady state are displayed in figure 7. Experiments testing the preservation of the steady state (2.12) showed that the

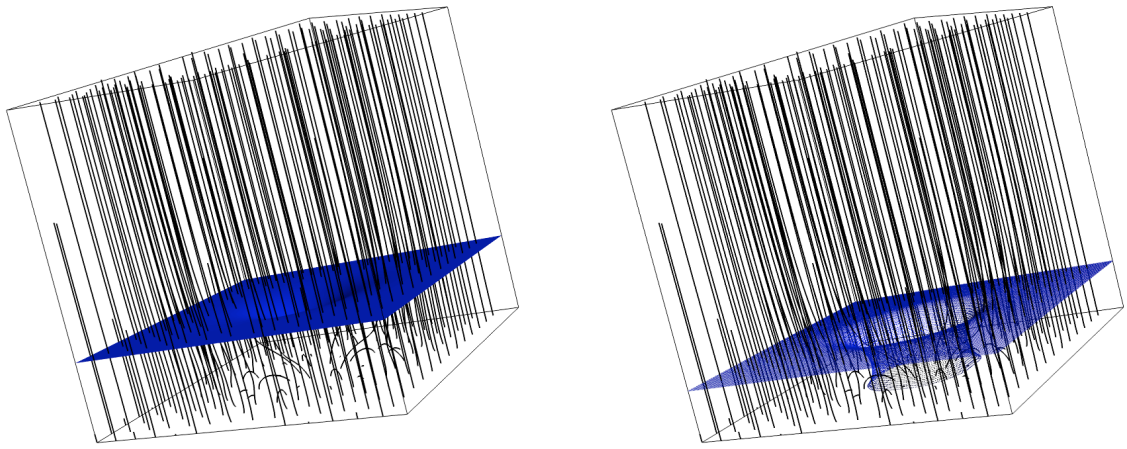

(a) weak field (b) strong field

FIGURE 7. 3-D magnetic field configurations with the $\beta = 1$ iso-surface shown in blue.

well-balanced schemes preserved a discrete version (3.40) of the steady state to machine precision. The errors for pressure were very similar to those shown in table 2 and we omit them here to concentrate on the wave propagation. The waves are induced as perturbations of the bottom boundary as in (4.4). We show results with the $H_{3\mathrm{WB}}M$ scheme only as the first-order results were quite dissipative. The waves are shown in figures 8 and 9 for the weak and strong field respectively. They reveal that the well-balanced scheme was quite robust in three dimensions and resolved the waves very sharply. The weak field results in figure 8 show that the magnetic field is not strong enough to focus the waves and the waves spread out spherically in the chromosphere. As the waves reach the $\beta = 1$ iso-surface, mode conversion takes place in a manner similar to two space dimensions. Further on, the waves reach the transition region and are accelerated. The temperature varies due to the waves and there are sinusoidal movements in the transition region.

On the other hand, the strong field in figure 9 focuses the waves in certain directions. These waves do not interact with the $\beta = 1$ iso-surface and reach the transition region, where they are accelerated by an order of magnitude. The movement of the transition region is more pronounced in this case. Both tests demonstrate the robustness of our schemes in three space dimensions and their ability to resolve the complex physics of wave propagation in a non-isothermal magneto-atmosphere.

5.1. **Simulations with observed data.** The above numerical experiments were performed with synthetic magnetic fields and bottom boundary conditions modeling the generation of waves. The real test of a code like SURYA is its performance on observed data sets. For this purpose, we present a three-dimensional simulation on an isothermal atmosphere (modeling only the chromosphere). The background magnetic field $\widetilde{\mathbf{B}}$ is given by (2.11) where the Fourier co-efficients are extracted from the magnetic field at the bottom boundary. Using the 3d data model of [13], measurements of the solar radial magnetic field by the MDI instrument on SOHO in 1997 are used to obtain the magnetic field at the bottom boundary. A fourier expansion of this *observed* field yields the co-efficients $\{a, b, c, d\}_{lm}$ which are used to define the background magnetic field by extrapolation as in (2.11). This *observed* background field is depicted in figure 10. The resulting magnetic field is very complex with a rather chaotic combination of open loop and closed loop field lines. In particular, there is a pronounced coming together of open field lines near the $y = 4$ axis where $(x, y, z) \in [0, 4] \times [0, 4] \times [0, 8]$ is the computational

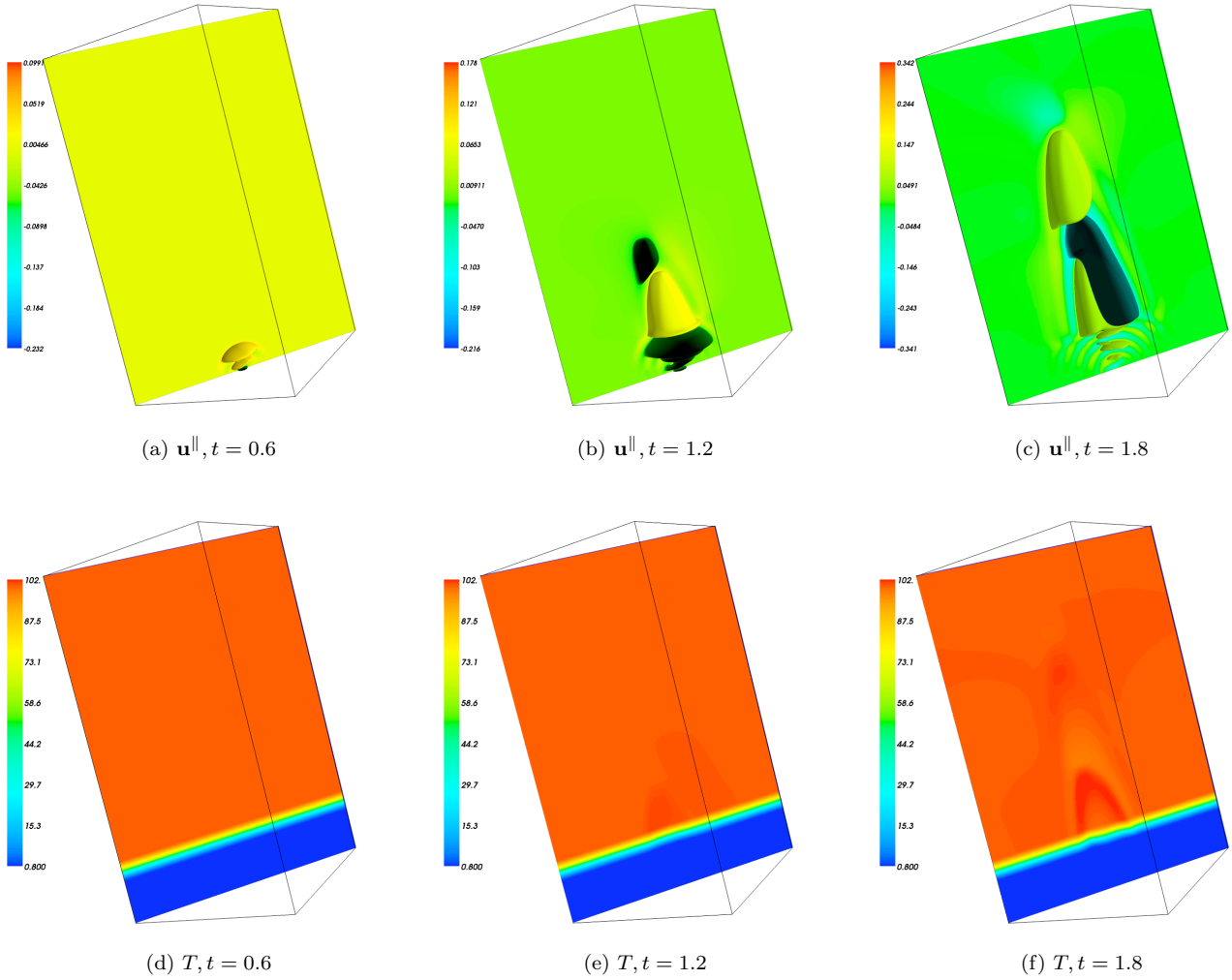

(a) $\mathbf{u}^{\parallel}, t = 0.6$ (b) $\mathbf{u}^{\parallel}, t = 1.2$ (c) $\mathbf{u}^{\parallel}, t = 1.8$

(d) $T, t = 0.6$ (e) $T, t = 1.2$ (f) $T, t = 1.8$

FIGURE 8. 3-D wave propagation with weak magnetic field on a $400 \times 400 \times 800$ mesh with $H_{3\mathrm{WB}}M$ scheme. Top: Iso-surfaces of $\mathbf{u}^{\parallel}$ and a two-dimensional slice. Bottom: Two-dimensional slice of temperature

domain. Other parts of the domain contain closed loop configurations. To add to the complexity, the boundary conditions at the bottom boundary, generating the waves, are from measurements of the radial velocity from the same area of the solar surface, and starting at the same time as the measurement of the magnetic field data, also using MDI. A time series of these velocity measurements is used. The resulting wave propagation on a $120 \times 60 \times 120$ mesh with the second-order $H_{3\mathrm{WB}}M$ scheme (the first order results were quite dissipative) are shown in figure 11. The figures show snapshots of the velocity in the direction of the magnetic field $\mathbf{u}^{\parallel}$ at six different time levels. The results illustrate the robustness of SURYA as it is able to handle observed data sets quite efficiently. The waves generated with observed bottom boundary conditions show quite complicated behavior in different parts of the domain. However, two features are quite pronounced: in those parts of the domain where the magnetic field is either weak or has a completely open topology (like near the $y = 0$ axis), the waves spread out and behave like hydrodynamic waves. On the other hand, in those parts of the domain (like near $x = 0, y = 4$) where the magnetic field is strong and there is a closed loop topology, the waves are focused by the field and follow the field lines as illustrated in figure 11. These results highlight the role of the

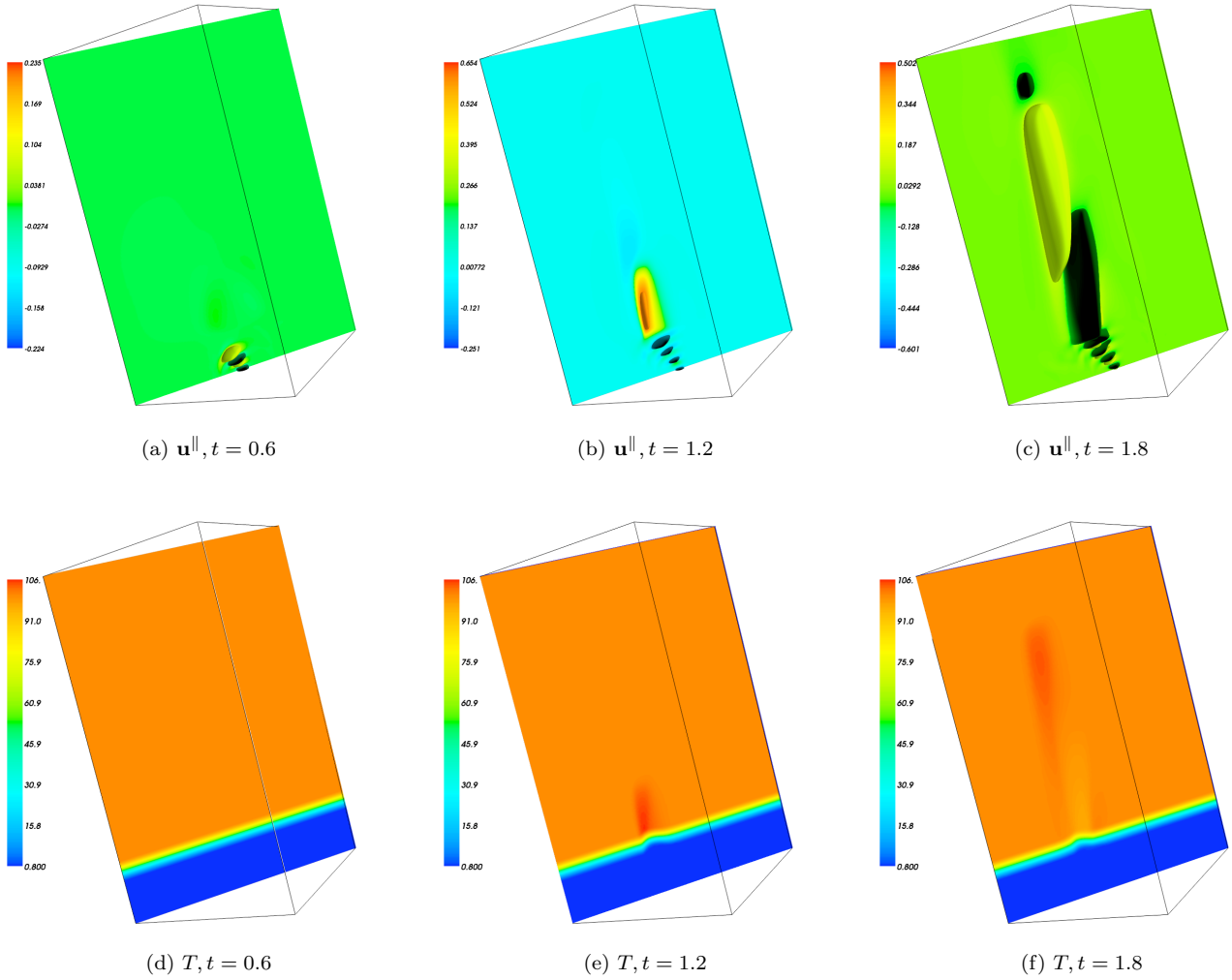

(a) $\mathbf{u}^{\parallel}, t = 0.6$ (b) $\mathbf{u}^{\parallel}, t = 1.2$ (c) $\mathbf{u}^{\parallel}, t = 1.8$

(d) $T, t = 0.6$ (e) $T, t = 1.2$ (f) $T, t = 1.8$

FIGURE 9. 3-D wave propagation with strong magnetic field on a $400 \times 400 \times 800$ mesh with $H_{3\mathrm{WB}}M$ scheme. Top: Iso-surfaces of $\mathbf{u}^{\parallel}$ and a two-dimensional slice. Bottom: Two-dimensional slice of temperature

magnetic field in shaping wave behavior quite well. The results presented here are preliminary and are intended to demonstrate the ability of the code to deal with very complicated realistic configurations. Detailed analysis of the results from a physics point of view will be considered in a forthcoming paper.

6. Conclusion

The paper follows [47, 7, 22] and considers the propagation of waves in idealized stratified magnetic atmospheres. The situation of interest is modeled by the equations of ideal MHD, augmented with a gravitational source term and suitable initial and boundary conditions. The waves are realized as perturbations of interesting steady states. In contrast to the aforementioned papers, we consider non-isothermal atmospheres with realistic steady state temperature distributions. Furthermore, the simulations are also carried out in three spatial dimensions.

The design of a robust and efficient numerical framework consists of the following ingredients:

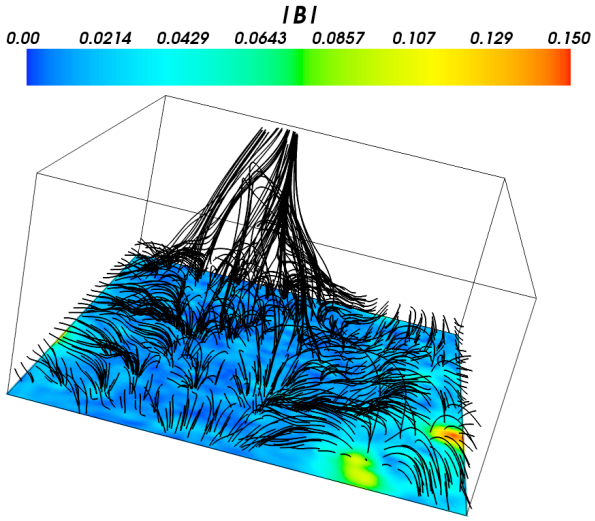

FIGURE 10. The background magnetic field for simulations with observed data.

- Using a version of the ideal MHD equations with embedded steady state potential magnetic fields.
- Stable HLL type three wave solvers for approximating the solutions of the resulting Riemann problems at each interface.
- Introducing and discretizing the Godunov-Powell source term in a novel *upwind* manner to handle the divergence constraint for multi-dimensional MHD.
- Suitable slope limiters and time stepping routines that lead to high-resolution finite volume schemes.
- Novel *scaled logarithmic* reconstruction of the pressure that leads to a *well-balanced* scheme and ensures the preservation of *any* discrete steady state of the form (3.40) for any arbitrary temperature distribution.
- Neumann type non-reflecting boundary conditions at the top vertical boundary.

All these ingredients are implemented in the form of a massively parallel C++ based code termed *SURYA*.

Numerical results from *SURYA* for two- and three-dimensional configurations are presented. These results demonstrate the crucial role played by the temperature variation in wave acceleration. Furthermore, the interaction between the waves and the magnetic field results in mode mixing and wave turning. Another highlight is the ability of the model and the code to resolve the motion of the transition region. The role of the magnetic field in shaping this transition is clearly brought out. Furthermore, we present results from test case based on background magnetic field and boundary conditions, observed by SOHO. The numerical results illustrate the robustness of the code as well as its ability to deal with and resolve very complicated physical processes and configurations.

As stated before, the model for wave propagation ignores vital energy transfer mechanisms like radiation. However, it is still able to highlight some of the dynamical mechanisms in stellar atmospheres. At the time of writing, radiation is being added as a module in SURYA and results will be presented in forthcoming papers.

REFERENCES

[1] E. Audusse, F. Bouchut, M. O. Bristeau, R. Klien and B. Perthame. A fast and stable well-balanced scheme with hydrostatic reconstruction for shallow water flows. *SIAM. J. Sci. Comput,* 25 (6), 2004, 2050 - 2065.

[2] J. Balbas and E. Tadmor. Non-oscillatory central schemes for one and two dimensional MHD equations II. High-order semi-discrete schemes. *SIAM J. Sci. Comput,* 28 (2), 2006, 533-560.

[3] D. S. Balsara and D. Spicer. A staggered mesh algorithm using high order Godunov fluxes to ensure solenoidal magnetic fields in magnetohydrodynamic simulations. *J. Comp. Phys.*, 149(2):270-292, 1999.

[4] T. J. Barth. Numerical methods for gas dynamics systems. *In An introduction to recent developments in theory and numerics for conservation laws*, D. Kröner, M. Ohlberger, C. Rohde (eds), Springer, 1999.

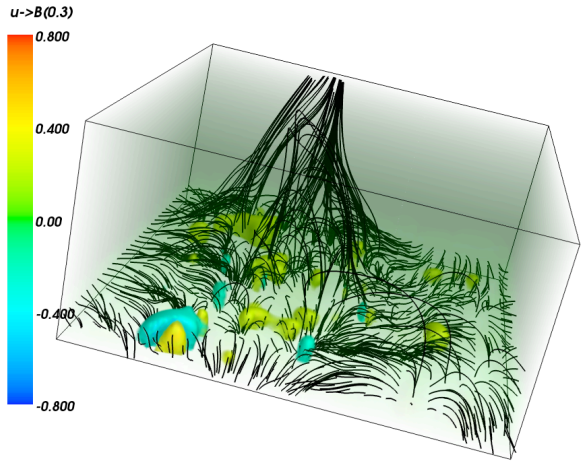

(a) $t = 0.3$

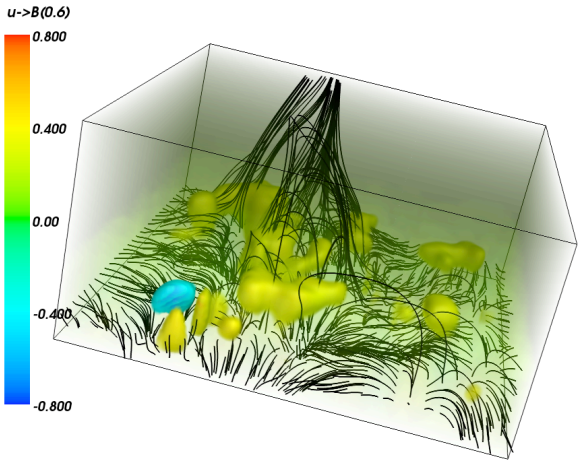

(b) $t = 0.6$

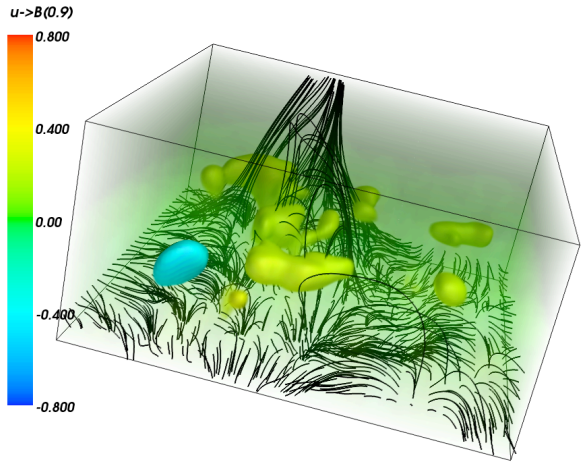

(c) $t = 0.9$

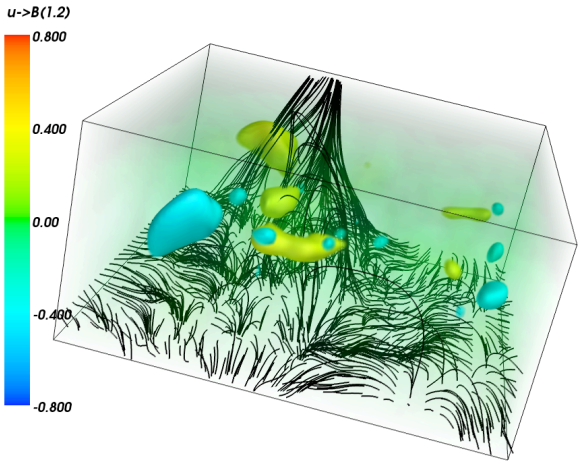

(d) $t = 1.2$

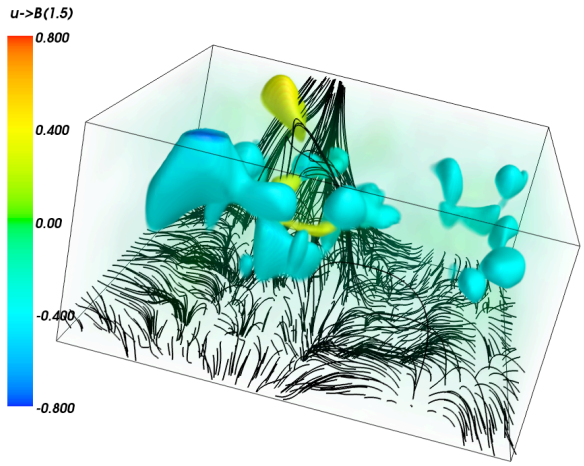

(e) $t = 1.5$

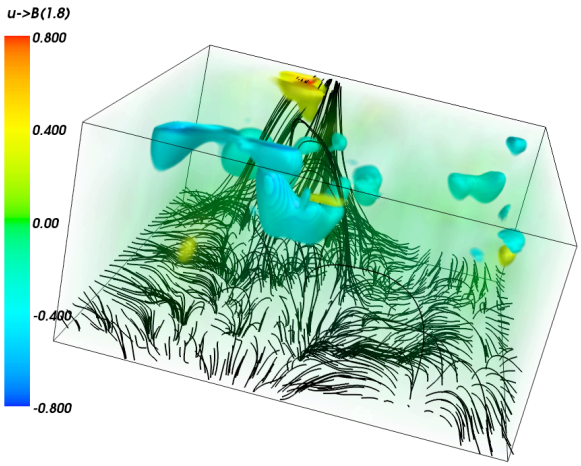

(f) $t = 1.8$

FIGURE 11. 3-D wave propagation with observed magnetic field and observed bottom boundary conditions (observations are from SOHO) on a $120 \times 60 \times 120$ mesh with $H_{3\text{WB}}M$ scheme. Each of the above figures show volumes of $\mathbf{u}^{\|}$ at different time instant.

[5] Christophe Berthon. Stability of the MUSCL Schemes for the Euler Equations, *Commun. Math. Sci.*, 3(2):133-157, 2005.
[6] D. Biskamp. Nonlinear magnetohydrodynamics. *Cambridge monographs on plasma physics*, Cambridge university press, 1993.
[7] T. J. Bogdan *et al*. Waves in the magnetized solar atmosphere II: Waves from localized sources in magnetic flux concentrations. *Astrophys. Jl,* 599, 2003, 626 - 660.
[8] F. Bouchut, C. Klingenberg and K. Waagan. A multi-wave HLL approximate Riemann solver for ideal MHD based on relaxation I- theoretical framework. *Numer. Math.*, 108 (1), 7-42, 2007.
[9] F. Bouchut, C. Klingenberg and K. Waagan. A multi-wave HLL approximate Riemann solver for ideal MHD based on relaxation II- Numerical experiments. *Preprint, 2008*.
[10] J. U. Brackbill and D. C. Barnes. The effect of nonzero div$B$ on the numerical solution of the magnetohydrodynamic equations. *J. Comp. Phys.*, 35:426-430, 1980.
[11] P. Cargo and G. Gallice. Roe matrices for ideal MHD and systematic construction of Roe matrices for systems of conservation laws. *J. Comp. Phys,* 136 (2), 1997, 446 - 466.
[12] M. Castro, J. M. Gallardo, C Parés. High order finite volume schemes based on reconstruction of states for solvving hyperbolic systems with non-conservative products. *Math. Comp.,* 75, 2006, 1103-1134.
[13] M. Carlsson and R. F. Stein. Wave Processes in the Solar Upper Atmsphere. in Magnetic Couple of the Solar Atmosphere, ed. H. Sawaya-Lacoste, *ESA SP-505*, 293-300, 2002.
[14] W. Dai and P. R. Woodward. A simple finite difference scheme for multi-dimensional magnetohydrodynamic equations. *J. Comp. Phys.*, 142(2):331-369, 1998.
[15] A. Dedner, F. Kemm, D. Kröner, C. D. Munz, T. Schnitzer and M. Wesenberg. Hyperbolic divergence cleaning for the MHD equations. *J. Comp. Phys.,* 175, 645-673, 2002.
[16] B. Einfeldt. On the Godunov type methods for gas dynamics. *SIAM. J. Num. Anal.*, 25 (2), 1988, 294 - 318.
[17] C. Evans and J. F. Hawley. Simulation of magnetohydrodynamic flow: a constrained transport method. *Astrophys. J.*, 332:659, 1998.
[18] F. Fuchs, K. H. Karlsen, S. Mishra and N.H. Risebro. Stable upwind schemes for the Magnetic Induction equation. *Preprint, Math. Model. Num. Anal,* to appear.
[19] F. Fuchs, S. Mishra and N. H. Risebro. Splitting based finite volume schemes for the ideal MHD equations. *J. Comp. Phys.,* 228 (3), 2009, 641-660.
[20] F. Fuchs, A. D. McMurry, S. Mishra, N. H. Risebro and K. Waagan. Finite volume schemes for wave propagation in stratified magneto-atmospheres. *Preprint 2008.*, Submitted, available from folk.uio.no/siddharm/art26.pdf
[21] F. Fuchs, A. D. McMurry, S. Mishra, N. H. Risebro and K. Waagan. Approximate Riemann solver based high-order finite volume schemes for the Godunov-Powell form of ideal MHD equations in multi-dimensions. *Preprint 2008.*, Submitted, available from folk.uio.no/siddharm/art32.pdf
[22] F. Fuchs, A. D. McMurry, S. Mishra, N. H. Risebro and K. Waagan Well-balanced high-order finite volume methods for simulating wave propagation in stratified magneto-atmospheres. *Preprint 2009.*, Submitted, available from folk.uio.no/siddharm/art37.pdf
[23] S. K. Godunov. The symmetric form of magnetohydrodynamics equation. *Num. Meth. Mech. Cont. Media*, 1:26-34, 1972.
[24] K. F. Gurski. An HLLC-type approximate Riemann solver for ideal Magneto-hydro dynamics. *SIAM. J. Sci. Comp.*, 25(6), 2004, 2165-2187.
[25] S. Gottlieb, C. W. Shu and E. Tadmor. High order time discretizations with strong stability property. *SIAM. Review,* 43, 2001, 89 - 112.
[26] A. Harten, B. Engquist, S. Osher and S. R. Chakravarty. Uniformly high order accurate essentially non-oscillatory schemes. *J. Comput. Phys.*, 1987, 231-303.
[27] K. H. Karlsen, S. Mishra and N.H. Risebro. A new class of well-balanced schemes for conservation laws with source terms, *Math. Comp.,* 78 (265), 2009, 55-78.
[28] K. H. Karlsen, S. Mishra and N.H. Risebro. Semi-Goudunov schemes for systems of conservation laws. *Ap. Num. Math.,* To appear, 2009.
[29] D. Kröner and M. D. Thanh. Numerical solutions to compressible flows in a nozzle with variable cross section. *SIAM. J. Numer. Anal.,* 43 (2) (2005), 796 - 824.
[30] S. Mishra and E. Tadmor. Constraint preserving schemes using potential-based fluxes. III. Genuinely multi-dimensional central schemes for MHD equations *Preprint 2009*, SAM research report 2009-33, SAM, ETH Zürich, Switzerland.
[31] P. G. LeFloch and M .D. Thanh. The Riemann problem for fluid flows in a nozzle with discontinuous cross-section. *Commun. Math. Sci.,* 1 (4), 2003, 763-797.
[32] R. J. LeVeque. Finite volume methods for hyperbolic problems. *Cambridge university press,* Cambridge, 2002.
[33] R. J. LeVeque. Balancing source terms and flux gradients in high-resolution Godunov methods: The quasi-steady wave-propagation algorithm *J. Comput. Phys.*, 146, 346 - 365, 1998.
[34] S. Li, An HLLC Riemann solver for magneto-hydrodynamics *J. Comput. Phys.* ,203,1,344-357,2005.
[35] T. J. Linde. *A three adaptive multi fluid MHD model for the heliosphere.* Ph.D thesis, University of Michigan, Ann-Arbor, 1998.
[36] P. Londrillo, L. del Zanna. On the divergence-free condition in Godunov-type schemes for ideal magnetohydrodynamics: the upwind constrained transport method. *J. Comput. Phys.* 195, 17-48, 2004.
[37] B. Marder A method for incorporating Gauss' law into electromagnetic pic codes. *J. Comput. Phys.*, 68 (1), 48-55, 1987.

[38] A. Mignone et. al. Pluto: A numerical code for computational astrophysics. *Astrophys. J. Suppl.*, 170, 2007, 228 - 242.
[39] S. Mishra. Analysis and Numerical Approximation of Conservation laws with discontinuous coefficients. *Ph.D thesis,* IISc, Bangalore, India, 2005, 260 pp.
[40] T. Miyoshi and K. Kusano. A multi-state HLL approximate Riemann solver for ideal magneto hydro dynamics. *J. Comp. Phys.* 208 (1), 2005, 315 - 344.
[41] S. Noelle, N. Pankratz, G. Puppo and J. Natvig. Well-balanced finite volume schemes of arbitrary order of accuracy for shallow water flows. *Journal of Computational Physics*, 213, 474-499, 2006.
[42] S. Noelle, N. Pankratz, G. Puppo and J. Natvig. Well-balanced finite volume schemes of arbitrary order of accuracy for shallow water flows. *Journal of Computational Physics*, 213, 474-499, 2006.
[43] T. J. Poinsot and S. K. Lele. Boundary conditions for direct simulations of compressible viscous flows. *J. Comp. Phys.* 101, 1992, 104 - 129.
[44] K. G. Powell. An approximate Riemann solver for magneto-hydro dynamics (that works in more than one space dimension). Technical report, 94 -24, ICASE, Langley, VA, 1994.
[45] K. G. Powell, P. L. Roe. T. J. Linde, T . I. Gombosi and D . L. De zeeuw, A solution adaptive upwind scheme for ideal MHD. *J. Comp. Phys*, 154(2), 284 - 309, 1999
[46] P. L. Roe and D. S. Balsara. Notes on the eigensystem of magnetohydrodynamics. *SIAM. J. Appl. Math.*, 56 (1), 1996, 57 - 67.
[47] C. S. Rosenthal *et al.* Waves in the magnetized solar atmosphere I: Basic processes and internetwork oscillations. *Astrophys. Jl,* 564, 2002, 508 - 524.
[48] J. Rossmanith. A wave propagation method with constrained transport for shallow water and ideal magnetohydrodynamics. Ph.D thesis, University of Washington, Seattle, 2002.
[49] D. S. Ryu, F. Miniati, T. W. Jones and A. Frank. A divergence free upwind code for multidimensional magnetohydrodynamic flows. *Astrophys. J.*, 509(1):244-255, 1998.
[50] C. W. Shu and S. Osher. Efficient implementation of essentially non-oscillatory schemes - II, *J. Comput. Phys.*, 83, 1989, 32 - 78.
[51] J. M. Stone et. al. Athena: A new code for astrophysical MHD. *Astrophys. J. Suppl.*, to appear. Preprint availabe on url:http://arxiv.org/abs/0804.0402.
[52] SURYA Available from http://folk.uio.no/mcmurry/amhd.
[53] T. Tanaka. Finite volume TDV scheme on an unstructured grid system for three-dimensional simulations of inhomogenous system including strong background potential field. *J. Comput. Phys.,* 111, 1994, 381.
[54] K. W. Thompson. Time dependent boundary conditions for hyperbolic systems. *J. Comp. Phys.*, 68, 1987, 1 - 24.
[55] M. Torrilhon. Locally divergence preserving upwind finite volume schemes for magnetohyrodynamic equations. *SIAM. J. Sci. Comp.*, 26(4):1166-1191, 2005.
[56] M. Torrilhon. Uniqueness conditions for Riemann problems of ideal Magneto-hydrodynamics. *J. Plasma. Phys.,* 69 (3), 253-276, 2003.
[57] G. Toth. The div$B = 0$ constraint in shock capturing magnetohydrodynamics codes. *J. Comp. Phys.*,161:605-652, 2000.
[58] B. Van Leer. Towards the ultimate conservative difference scheme. V. *J. Comp. Phys.*, 32, 101-136, 1979.
[59] K. Waagan. A positive MUSCL-Hancock scheme for ideal MHD. *Preprint, 2008.*

(Franz Georg Fuchs) Centre of Mathematics for Applications (CMA)
University of Oslo
P.O. Box 1053, Blindern
N–0316 Oslo, Norway
E-mail address: franzgeorgfuchs@gmail.com
URL: http://folk.uio.no/franzf/

(Andrew D. McMurry) Centre of Mathematics for Applications (CMA)
University of Oslo
P.O. Box 1053, Blindern
N–0316 Oslo, Norway
E-mail address: a.d.mcmurry@ifi.uio.no

(Siddhartha Mishra) Seminar for Applied Mathematics (SAM)
ETH Zürich,
Rämistrasse 101,
Zürich-8044, Switzerland
E-mail address: siddharm@cma.uio.no

(Knut Waagan) Center for scientific computation and mathematical modeling (CSCAMM)
University of Maryland,
CSIC Building 406,
College park MD:20742-3289, U.S.A
E-mail address: kwaagan@cscamm.umd.edu

Research Reports

No.	Authors/Title
10-27	*F.G. Fuchs, A.D. McMurry, S. Mishra and K. Waagan* Well-balanced high resolution finite volume schemes for the simulation of wave propagation in three-dimensional non-isothermal stratified magneto-atmospheres
10-26	*U.S. Fjordholm, S. Mishra and E. Tadmor* Well-balanced, energy stable schemes for the shallow water equations with varying topography
10-25	*U.S. Fjordholm and S. Mishra* Accurate numerical discretizations of non-conservative hyperbolic systems
10-24	*S. Mishra and Ch. Schwab* Sparse tensor multi-level Monte Carlo finite volume methods for hyperbolic conservation laws with random intitial data
10-23	*J. Li, J. Xie and J. Zou* An adaptive finite element method for distributed heat flux reconstruction
10-22	*D. Kressner* Bivariate matrix functions
10-21	*C. Jerez-Hanckes and J.-C. Nédélec* Variational forms for the inverses of integral logarithmic operators over an interval
10-20	*R. Andreev* Space-time wavelet FEM for parabolic equations
10-19	*V.H. Hoang and C. Schwab* Regularity and generalized polynomial chaos approximation of parametric and random 2nd order hyperbolic partial differential equations
10-18	*A. Barth, C. Schwab and N. Zollinger* Multi-Level Monte Carlo Finite Element method for elliptic PDE's with stochastic coefficients
10-17	*B. Kågström, L. Karlsson and D. Kressner* Computing codimensions and generic canonical forms for generalized matrix products
10-16	*D. Kressner and C. Tobler* Low-Rank tensor Krylov subspace methods for parametrized linear systems